East European Journal of Physics. 4. 112–132 (2025)
DOI: 10.26565/2312-4334-2025-4-10 ISSN 2312-4334

EXTENSION FROM CORE TO NO-CORE NUCLEAR SHELL MODEL WITH HARTREE–FOCK WAVE FUNCTION: APPLICATION TO POSITIVE-PARITY STATES IN ^{19}F

Berun N. Ghafoor[1*,2], **Aziz H. Fatah**[3], **Ari K. Ahmed**[1]
[1] *University of Sulaimani, College of Education, Physics department, Iraq*
[2] *Research and Development Center, University of Sulaimani, Iraq*
[3] *University of Sulaimani, College of Science, Physics department, Iraq*
[*] *Corresponding Author e-mail: berun.ghafoor@univsul.edu.iq*

Received July 7, 2025; revised September 9, 2025; accepted September 27, 2025

This work presents a detailed investigation of low-lying positive-parity states in the ^{19}F nucleus by combining shell-model techniques with Hartree–Fock (HF) calculations. The study systematically extends from traditional core-based spaces (*sd*, *zbm*, *psd*) to the fully untruncated no-core configuration (*spsdpf*). Realistic single-particle wavefunctions were generated using harmonic oscillator (HO), Woods–Saxon (WS), and Skyrme parameterizations. The approach was tested across a broad set of observables, including excitation spectra, electromagnetic form factors ($C0$, $C2$, $C4$, $M1$, $M3$, $E2$, $E4$, and $E4 + M5$), transition probabilities, magnetic dipole and electric quadrupole moments, as well as binding energies and rms charge radii. Discrepancies reported in earlier theoretical work, particularly for the $M1$ and $C4$ transitions at higher momentum transfers, were resolved through expanded model spaces and refined radial wavefunctions. Together with our previous study of negative-parity states in ^{19}F, these results provide a coherent picture: systematic core-to-no-core extensions are essential for accurately reproducing both detailed and bulk nuclear properties. This unified framework strengthens theoretical modeling of ^{19}F and establishes a foundation for future shell-model studies of nuclei in transitional and deformed regions.

Keywords: *Nuclear shell model; No-core shell model; Hartree–Fock wave function; Skyrme Hartree–Fock; Effective interaction; Electromagnetic form factors; Energy levels of* ^{19}F

PACS: 21.60.Cs, 21.60.Jz, 25.30.Bf, 21.10.-k, 27.20.+n

1. INTRODUCTION

The ^{19}F nucleus is an excellent example of a light, odd-A, strongly deformed nuclear system of sufficient size and complexity to exhibit properties of a many-body system. Electron scattering, through its well-understood electromagnetic interaction, serves as a powerful probe of the nuclear structure. In this work, nuclear structure properties were investigated using the shell model and the Hartree–Fock method, with core-to-no-core extensions enhancing theoretical reliability. This technique focuses on increasing the number of valence particles to investigate the static and dynamic structure of ^{19}F. Within the recent progress of shell model research areas, the necessity to choose and apply a model space as well as effective interactions crucial in identifying and explaining nuclear structure phenomena has become evident. Ghafoor et al. [1] compared the excitation of negative parity states in ^{19}F using core and no-core shell models and their calculations have shown that adding the no-core leads to much better agreement with the observables especially in transition strengths and energy spectra. Correspondingly, Ryssens and Alhassid [2] developed the HF-SHELL code that implements finite-temperature Hartree-Fock algorithms to tackling shell model Hamiltonians and discussed its applicability to the statistical and collective properties of nuclei at high excitation. These were supplemented by Saxena and Srivastava [3] who performed first-principles calculations using an *ab initio* no-core shell model to gain insight into neutron-rich $^{18-23}$O and $^{18-24}$F isotopes, and indicated that structure experimentalists may expect first-principles studies of such systems to employ large model spaces to resolve detail in such systems.

Large-scale shell model predictions of Jassim and Sahib [4] have also been provided on ^{19}F, as well as the adjoining nuclei, such as ^{25,26}Mg and ^{27}Al, demonstrating that concomitant conventions of interaction-model spaces can produce solid spectra and electromagnetic properties. Similarly, Singh et al. [5] demonstrated that complete shell model calculations of even and odd A nuclei in several mass regions could effectively reproduce calculated and experimental energy levels, form factors, and transition moments, in the case of high-quality interactions being used. Taken together, these works support the generality of the shell model in understanding nuclear structure and support the tendency to use the traditional shell model frameworks along with more modern treatments, i.e., *ab initio* methods and mean-field approximations, to improve our knowledge of light and medium-mass nuclei.

The development of recent years with the study of nuclear structure of sd-shell nuclei has significantly relied on the method of configuration-interaction shell model to investigate the electromagnetic response and electron scattering processes. The study of Le Noan and Sieja [6] explored the electric dipole response of sd-shell nuclei and determined

Cite as: B.N. Ghafoor, A.H. Fatah, A.K. Ahmed, East Eur. J. Phys. 4, 112 (2025), https://doi.org/10.26565/2312-4334-2025-4-10

that the collective and single-particle excitations of light nuclei are important through the shell-model description with well-selected effective interactions that reproduce well their low-energy dipole strength distributions.

In connection with these results, Radhi *et al.* performed shell model calculations in detail of the electron scattering of the ^{19}F nucleus, both positive and negative parity of the states. In their work [7], they found that inelastic scattering form factors can be successfully described using shell-model wave functions, including realistic configuration mixing, which allowed insight into nuclear excitation mechanisms and the densities of transition states. Radhi, Abdullah, and Raheem [8] first applied these analyses with no-core shell model wave functions of a large basis, which gave a better match to elastic and inelastic measurements of electron scattering and emphasized the need to include the complete model space in a description.

The rationales of these computational works lie in the development of effective interactions as advanced by Smirnova *et al.* [9] in the sd shell. They formulated and tested improved sets of new interactions that improve the predictive capability of shell-model calculations, in particular, on spectroscopy and transition strengths, thus allowing a more precise description of the experimental observables in all the nuclei of the sd-shell.

Brown *et al.* [10] conducted a detailed shell-model analysis of high-resolution elastic and inelastic electron scattering data for ^{19}F, successfully reproducing key longitudinal and transverse form factors for both positive- and negative-parity states. Their study demonstrated the utility of the *sd*-shell configurations and limited cross-shell excitations in capturing essential electromagnetic observables. However, the analysis was constrained by truncated model spaces, reliance on a fixed effective interaction, and the use of phenomenological single-particle wavefunctions. These limitations restricted the treatment of configuration mixing and reduced the accuracy of predictions at higher momentum transfers—especially for complex multipole components. Furthermore, the absence of systematic uncertainty quantification and the exclusion of extended model spaces, such as the *pf*-shell, limited the completeness and generalizability of the results, indicating the need for modern no-core approaches and diverse interaction benchmarking for deeper nuclear structure insight.

In combination, such studies reveal the configuration-interaction shell model using extended effective interactions to be a formidable theoretical instrument in the study of nuclear electromagnetic responses in sd-shell nuclei, especially using observables in electron scattering as the sensitive probe of nuclear structure.

The present investigation evaluates the energy spectra, reduced transition probabilities, magnetic dipole moments, nuclear root-mean-square radii, binding energy, and both longitudinal and transverse inelastic electron scattering form factors for the ^{19} F nucleus. The analysis utilizes four distinct model spaces to systematically examine the influence of progressively extending the core configuration, culminating in a no-core framework, on the calculated nuclear properties and scattering observables

2. THEORETICAL FORMALISM

To investigate the nuclear structure properties of ^{19}F, we employed both the shell model and the Hartree–Fock (HF) approaches. Each method was carefully implemented using relevant effective interactions and computational tools, and all mathematical formulations were consistently applied throughout the study.

In the HF method, the wave function of a nucleus $|\psi_{\rm HF}\rangle$, consisting of A nucleons, can be written as a Slater determinant of single-particle wave functions ϕ_i [11, 12]:

$$|\psi_{\rm HF}(u_1,u_2,\ldots,u_A)\rangle = \frac{1}{\sqrt{A!}}\begin{vmatrix}\phi_1(u_1) & \cdots & \phi_1(u_A)\\ \vdots & \ddots & \vdots\\ \phi_A(u_1) & \cdots & \phi_A(u_A)\end{vmatrix}, \tag{1}$$

where $u_i = (\vec{r},\sigma,t_z)$ includes spatial coordinates $\vec{r}$, spin projection σ, and isospin projection t_z ($+1/2$ for proton, $-1/2$ for neutron). The HF method minimizes the expectation value of the total Hamiltonian [13]:

$$\hat{H} = -\frac{\hbar^2}{2m}\sum_{i=1}^{A}\nabla^2 + \hat{V}_{\rm Skyrme}, \tag{2}$$

where the Skyrme effective interaction [14] models the mean-field behavior of nucleons through zero-range, density-dependent forces:

$$\hat{V}_{\rm Skyrme} = \sum_{i<j}V_{ij}^{(2)} + \sum_{i<j<k}V_{ijk}^{(3)}. \tag{3}$$

The two-body component consists of central, spin-orbit, and tensor terms [14, 15, 16]:

$$\hat{V}_{\rm Skyrme}(\vec{r}_1,\vec{r}_2) = \hat{V}^m + \hat{V}^{LS} + \hat{V}^t, \tag{4}$$

with

$$\hat{V}^m = t_0(1+x_0\hat{P}_\sigma)\delta_{12} + \frac{t_1}{2}(1+x_1\hat{P}_\sigma)(\hat{k}_1^2+\hat{k}_2^2)\delta_{12}$$

$$+ t_2(1 + x_2\hat{P}_\sigma)\hat{k}_2 \cdot \hat{k}_1\delta_{12} + \frac{t_3}{6}(1 + x_3\hat{P}_\sigma)\rho^\alpha(r)\delta_{12}, \tag{5}$$

$$\hat{V}^{LS} = it_4(\hat{\sigma}_1 + \hat{\sigma}_2) \cdot (\hat{k}_2 \times \hat{k}_1)\delta_{12}, \tag{6}$$

$$\begin{aligned}\hat{V}^t = \frac{t_e}{2}\Big[&3(\hat{\sigma}_1 \cdot \hat{k}_2)(\hat{\sigma}_2 \cdot \hat{k}_2) - (\hat{\sigma}_1 \cdot \hat{\sigma}_2)\hat{k}_2^2 \\ &+ 3(\hat{\sigma}_1 \cdot \hat{k}_1)(\hat{\sigma}_2 \cdot \hat{k}_1) - (\hat{\sigma}_1 \cdot \hat{\sigma}_2)\hat{k}_1^2\Big]\delta_{12} \\ &+ t_s[3(\hat{\sigma}_1 \cdot \hat{k}_2)(\hat{\sigma}_2 \cdot \hat{k}_1) - (\hat{\sigma}_1 \cdot \hat{\sigma}_2)(\hat{k}_2 \cdot \hat{k}_1)^2]\delta_{12},\end{aligned} \tag{7}$$

where $\delta_{12} = \delta(\vec{r}_1 - \vec{r}_2)$ is the Dirac delta function. The operators $\hat{k}_1 = \frac{1}{2i}(\vec{\nabla}_1 - \vec{\nabla}_2)$ and $\hat{k}_2 = -\frac{1}{2i}(\vec{\nabla}_1 - \vec{\nabla}_2)$ act on the right and left wavefunctions, respectively. The three-body force is simplified as

$$V^{(3)}_{\text{Skyrme}} = t_3\delta_{12}\delta_{13}. \tag{8}$$

The radial part of the single-particle wavefunctions is [15, 16]:

$$\phi_{nljm}(r) = \frac{R_{nl}(r)}{r}Y_{jlm}(\Omega_r), \tag{9}$$

with the corresponding density distributions [11]:

$$\rho_s(r) = \sum_{n_\alpha, j_\alpha, l_\alpha} \omega_\alpha \frac{(2j_\alpha + 1)}{4\pi}\left(\frac{R^{(s)}_{n_\alpha l_\alpha}(r)}{r}\right)^2, \tag{10}$$

and root-mean-square (rms) radii [17, 18]:

$$r_s = \langle r_s^2\rangle^{1/2} = \left[\frac{\int dr\, r^4\rho_s(r)}{\int dr\, r^2\rho_s(r)}\right]^{1/2}. \tag{11}$$

In the shell model, electromagnetic form factors are calculated via reduced matrix elements. The one-body transition densities (OBTDs), computed using the NuShellX code [19], are defined as

$$\text{OBDM}_{J,t_z}(J_i, J_f) = \frac{\langle J_f\|[a^\dagger_\alpha \otimes \tilde{a}_\beta]^J\|J_i\rangle}{\sqrt{2J + 1}}. \tag{12}$$

The reduced matrix element is then [20]:

$$\langle J_f\|\hat{T}^\eta_{J,t_z}(q)\|J_i\rangle = \sum_{\alpha,\beta}\text{OBDM}_{J,t_z}(J_i, J_f)\langle\alpha\|\hat{T}^\eta_{J,t_z}(q)\|\beta\rangle, \tag{13}$$

and the form factor squared is [21]:

$$|F^J_\eta(q)|^2 = \frac{4\pi}{Z^2(2J_i + 1)}\left|\sum_{t_z} e(t_z)\langle J_f\|\hat{T}^\eta_{J,t_z}(q)\|J_i\rangle\right|^2 |F_{\text{cm}}(q)|^2|F_{\text{fs}}(q)|^2, \tag{14}$$

where the center-of-mass and finite-size corrections are [22]

$$|F_{\text{cm}}(q)| = \exp\left(\frac{b^2q^2}{4A}\right), \tag{15}$$

$$|F_{\text{fs}}(q)| = \exp\left(-\frac{0.43q^2}{4}\right). \tag{16}$$

The longitudinal and transverse form factors are [20, 21]

$$|F_L(q)|^2 = \frac{1}{2J_i + 1}\sum_{J\geq 0}|\langle J_f\|\hat{T}^C_{J,t_z}(q)\|J_i\rangle|^2, \tag{17}$$

$$|F_T(q)|^2 = \frac{1}{2J_i + 1}\sum_{J\geq 1}\left\{|\langle J_f\|\hat{T}^E_{J,t_z}(q)\|J_i\rangle|^2 + |\langle J_f\|\hat{T}^M_{J,t_z}(q)\|J_i\rangle|^2\right\}, \tag{18}$$

and the total form factor in plane-wave Born approximation (PWBA) is [20, 21]

$$|F(q,\theta)|^2 = \left(1 - \frac{\omega^2}{q^2}\right)|F_L(q)|^2 + \left[\frac{1}{2}\left(1 - \frac{\omega^2}{q^2}\right) + \tan^2\left(\frac{\theta}{2}\right)\right]|F_T(q)|^2. \tag{19}$$

Finally, the reduced transition probability is given by [21]:

$$B(\eta J) = \frac{Z^2}{4\pi}\left[\frac{(2J+1)!!}{k^J}\right]^2 |F_J^{\eta}(k)|^2, \tag{20}$$

where $k = E_x/\hbar c$ is the momentum transfer corresponding to the excitation energy.

3. RESULT AND DISCUSSION

Building upon our earlier study [1], where the root mean square (rms) charge radius and binding energy of ^{19}F were successfully reproduced using a single Skyrme-Hartree–Fock parameterization (SLy4), the present work marks a significant methodological advancement. While the previous calculation yielded results in strong agreement with experiment—2.876 fm for the rms radius and 146.372 MeV for binding energy—this study systematically expands the scope by employing an extensive set of thirty-nine Skyrme interactions. These are analyzed in parallel with harmonic oscillator (HO) and Woods–Saxon (WS) potentials to rigorously evaluate their effectiveness in reproducing key nuclear observables. This enriched comparative framework enables a more robust benchmarking of global nuclear properties and provides deeper insight into the sensitivity of model predictions to mean-field structure.

In addition to global quantities, the present investigation delves into the fine structure of low-lying positive parity states in ^{19}F by analyzing longitudinal and transverse electron scattering form factors, electromagnetic transition probabilities, magnetic and quadrupole moments, and excitation spectra. The study is structured around a progressive extension of the shell model space, beginning with the conventional *sd*-shell (based on an ^{16}O core) and expanding through the *zbm* (^{12}C core), *psd* (^{4}He core), and fully untruncated *spsdpf* no-core model. This hierarchical modeling strategy, combined with realistic single-particle wavefunctions from Hartree–Fock and alternative potentials, allows for a critical evaluation of how model space and interaction choices affect the reproduction of experimental data.

The present study is a significant development in the theory of nuclear structure and very far beyond the earlier applications of the shell model, like Radhi et al. [7, 8] and Brown [10]. Unlike earlier studies that were limited to truncated core configurations and narrow interaction sets, we implemented a systematic core-to-no-core shell model framework, treating all 19 nucleons of ^{19}F as dynamically active in the most extended model space cause to reproduce some observable that is better than previous studies.

The results are presented in order of increasing angular momentum, offering a clear and coherent narrative of the evolving nuclear structure across multiple observables.

Angular momentum and parity conservation allow only certain multipole parts, namely $C0$, $E0$ and $M1$ for Coulomb, transverse electric and transverse magnetic form factors respectively for ground state. The time-reversal symmetry removes the $E0$ component though. The elastic Coulomb $C0$ form factors of the ground state of the nucleus ^{19}F ($1/2^+$, 0 MeV) were calculated with the help of shell-model wave functions related to model spaces *sd*, *zbm*, *psd* and *spsdpf*. These were coupled to radical single-particle wavefunctions, of Skyrme Hartree–Fock parameterization (SkXcsb, SkXta, SkXtb, SLy4), Woods–Saxon (WS) and harmonic oscillator (HO) potentials. The constructed fit is compared to the experimentally measured form-factor in the Ref. [10] as the benchmark data presented in Fig. 1.

For the momentum transfer region $q = 0$ to 1.6 fm^{-1}, all model spaces, ranging from extended-core to no-core configurations, demonstrate good agreement with experimental data across all potential types. The C0 form factor near $q = 1.57$ fm^{-1} up to 3 fm^{-1}, calculated using the Woods–Saxon potential, aligns closely with experimental data for both the *sd*- and *psd*-model spaces (core configurations of ^{16}O and ^{4}He, respectively). This strong similarity between the two model spaces may be attributed to the clustering of ^{16}O as four ^{4}He nuclei. For the ^{12}C core with the ZBMI interaction, the C0 form factor achieves optimal agreement with experimental data using the Woods–Saxon potential in the q-value regions 1.57–1.61 fm^{-1} and 2.28–2.4 fm^{-1}. In the intermediate range 1.61–2.28 fm^{-1}, the SkXcsb Skyrme potential produces the most accurate results. For the final two experimental q-values obtained using no-core calculations, both HO and WS potentials yield results in good agreement with the experimental data [10].

Unlike previous works, our study is the first to systematically reproduce the longitudinal $C0$ form factor of the ground state $1/2^+_1$ throughout the entire momentum transfer range using all core and no-core model spaces (*sd*, *zbm*, *psd*, and *spsdpf*), demonstrating that the charge distribution of the ground state can be robustly captured regardless of the core truncation, a result not previously

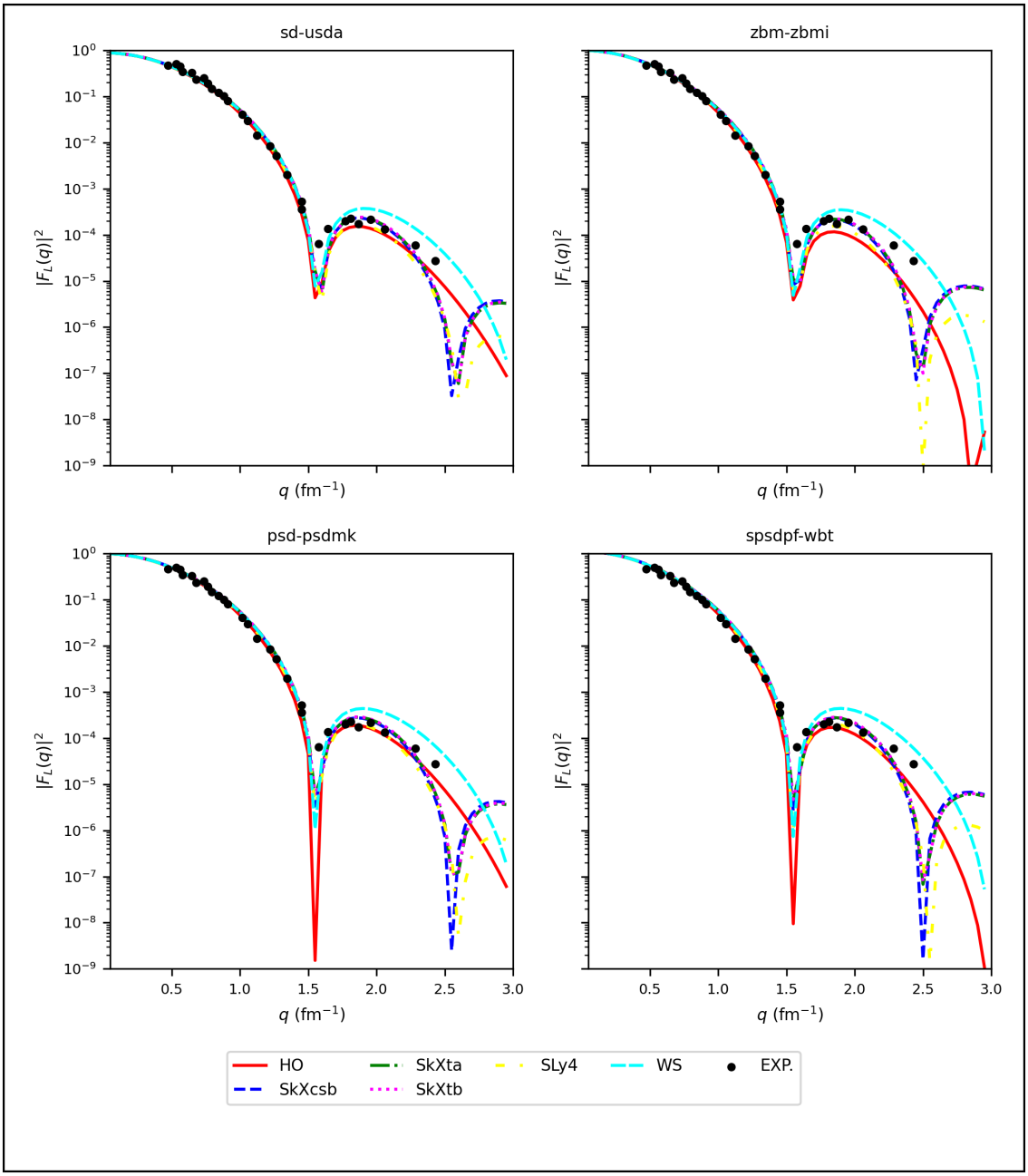

Figure 1. Elastic Coulomb C0 form factor for the $1/2^+$ ground state of ^{19}F, calculated using various model spaces and radial potentials. Theoretical predictions are compared to experimental data from Ref. [10].

The transverse magnetic M1 form factors are presented in Fig. 2. A high level of consistency is observed between the experimental results and the calculations using all the employed potentials in the momentum transfer range, particularly with the *sd*-shell wavefunction and ^{16}O core. However, in the region q = 1.2–1.7 fm^{-1}, the calculated form factors are underestimated. In particular, within this momentum transfer range, five out of the six potentials employed, excluding SkXcsb, exhibit qualitative agreement with the experimental M1 form factor data. The measurements reveal two diffraction minima located at q = 1.1 fm^{-1} and q = 1.6 fm^{-1}, though these features appear slightly shifted in the theoretical predictions. Among all potentials, the Woods–Saxon (WS) potential (represented by cyan dashed) provides the closest match to the experimental data in the region q = 1.49–1.57 fm^{-1}.

For the ($^{12}_{6}$C) core configuration using the ZBMI interaction—where only seven valence nucleons are active—all potentials qualitatively reproduce the M1 form factors. However, the SLy4 Skyrme potential (dotted line) delivers the best overall agreement, though it fails to precisely replicate the observed minima near q = 1.57 fm^{-1}. When employing the ($^{2}_{4}$He) core within the psd-model space and the PSDMK interaction, the M1 form factors show excellent agreement with the experimental data. The diffraction minima are best reproduced using the harmonic oscillator (HO) and WS potentials, especially around q = 1.49 fm^{-1}, where all Skyrme potentials and the HO curve intersect this crucial point.

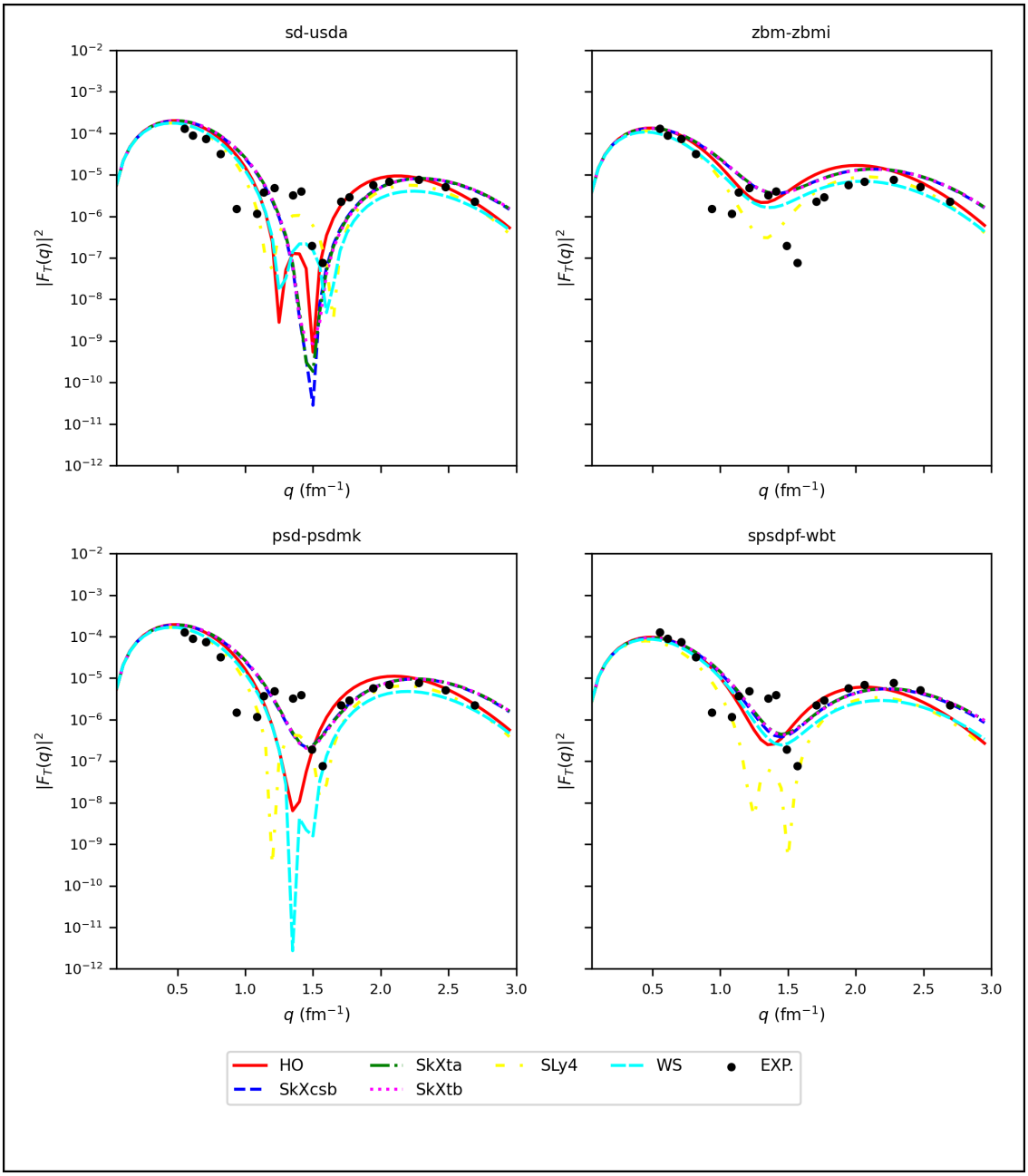

Figure 2. Theoretical transverse form factor $M1$ for the $1/2_1^+$ state in comparison with experimental data from Refs. [10, 23].

In the range q = 1.7–2.23 fm^{-1}, the transverse M1 form factors calculated within the psd-model space align most accurately with experimental values when Skyrme potentials are employed. At even higher momentum transfers (q = 1.7–3 fm^{-1}), the HO and WS potentials yield the best fits, while the SLy4 potential achieves only partial agreement.

Finally, for the fully untruncated *spsdpf* model space (no-core configuration) using the WBT interaction, all potentials—with the exception of SLy4—show excellent agreement across the entire M1 form factor momentum range. Interestingly, the SLy4 potential still provides strong agreement at the critical point q = 1.57 fm^{-1}.

In contrast to Brown et al. [10], who failed to reproduce the transverse $M1$ form factor of the $1/2_1^+$ state—especially at low momentum transfers—our approach not only recovers both diffraction minima but also achieves excellent agreement across all momentum ranges using the *sd* and *psd* model spaces with HO and WS potentials, while the no-core *spsdpf* calculations uniquely resolve the second minimum using the SLy4 Skyrme interaction, marking a major improvement in modeling the magnetic structure of the ground state.

The Coulomb contribution $C2$ for the $3/2_1^+$ state, as depicted in Fig. 3, demonstrates remarkable consistency between the *sd*-shell wavefunction calculations and experimental data across all q-values, with only minor overestimations.

However, the first minimum at approximately $q = 1.75$ fm^{-1} is qualitatively well reproduced by the HO potential and is quantitatively closer when using the SLy4 parameterization. In the range $q = 2$–2.4 fm^{-1}, the HO potential provides a notably better fit than the other parameterizations.

For the *zbm*-model space, the form factors exhibit good qualitative agreement across all q-values, albeit with a systematic shift. The minimum point is quantitatively well reproduced by both the HO and WS potentials, while the Skyrme parameterizations (SkXcsb, SkXta, SkXtb, and SLy4) excel qualitatively in this momentum transfer range. The suppression of the transverse $C2$ form factor for the $3/2^+_1$ state using the zbm-ZBMI interaction is attributed to its significant overestimation of the excitation energy, as shown in Fig. 11. This suggests an inadequately configured wavefunction for this state, lacking essential configuration mixing and collectivity.

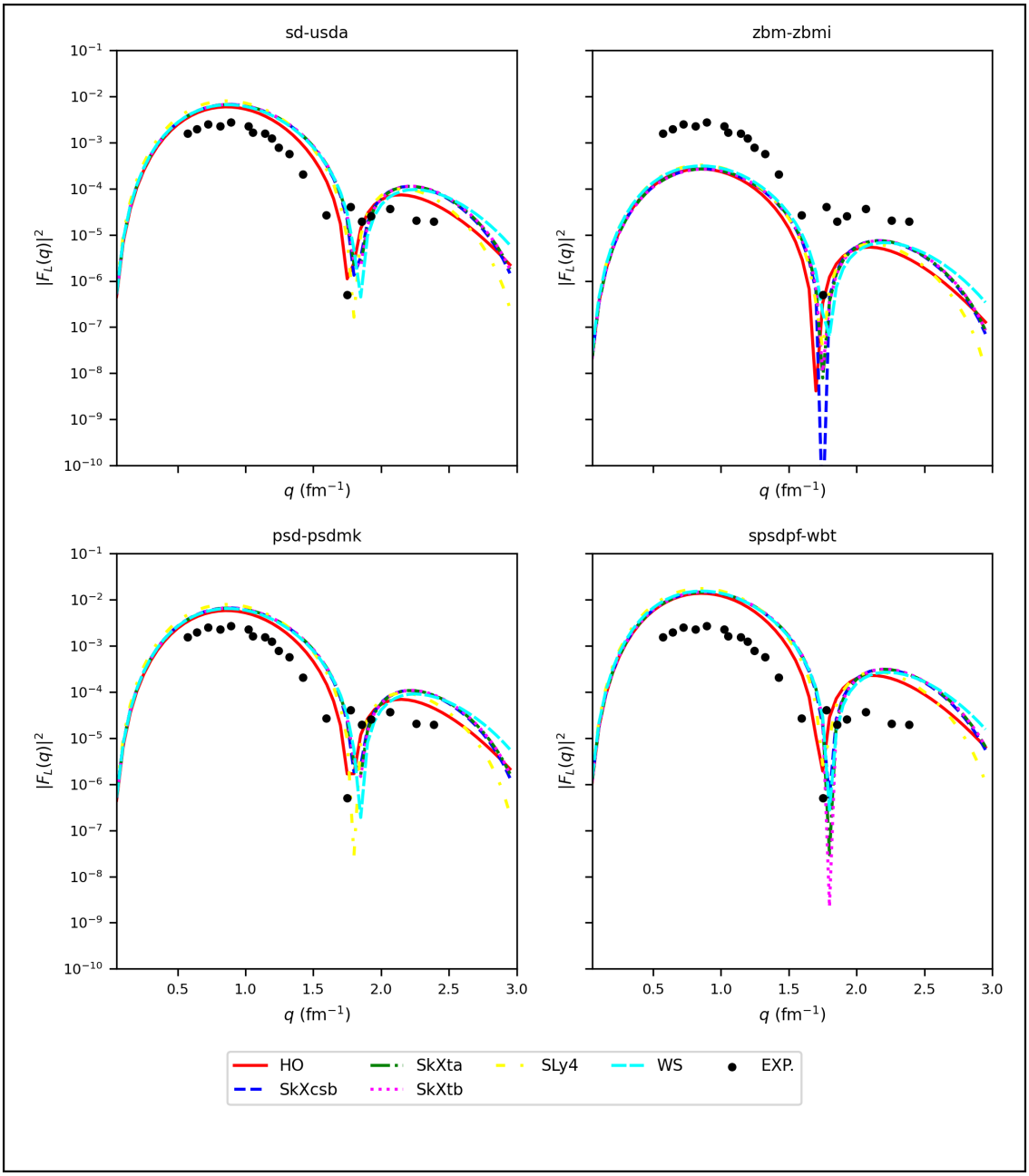

Figure 3. Theoretical longitudinal form factor $C2$ for $3/2^+_1$ compared with experimental data [10, 24].

The *zbm* model space, based on a ^{12}C core ($Z = N = 6$), does not benefit from the enhanced stability of a doubly magic configuration, thereby limiting the accuracy of transition strength predictions. Consequently, the reduced transition density leads to an under prediction of the form factor strength in Fig. 3.

The results for the *psd*-model space are strikingly similar to those from the *sd*-shell wavefunction, further reinforcing the idea that the $^{16}_{8}$O core can emerge as a cluster derived from the $^{4}_{2}$He core. Notably, the PSDMK interaction [25],

developed from the PW interaction within the *sd*-model space, incorporates the active $1d_{5/2}$, $2s_{1/2}$, and $1d_{3/2}$ orbitals above an inert $^{16}_{8}$O core.

Finally, within the *spsdpf*-model space, all potentials demonstrate exceptional agreement with the experimental $C2$ form factors across the entire q-value range, surpassing the accuracy of the other model spaces. This finding confirms that no-core shell model calculations are the most effective method for investigating form factors using an advanced shell model framework, where all nucleons are actively interacting.

Additionally, the no-core calculations reveal that the SkXcsb, SkXta, and SkXtb parameterizations yield similar results, while the SLy4 potential shows excellent agreement with WS and nearly with the HO potential. The differences among these potentials arise primarily from the renormalization of the $2s1d$ single-particle matrix elements within the model spaces.

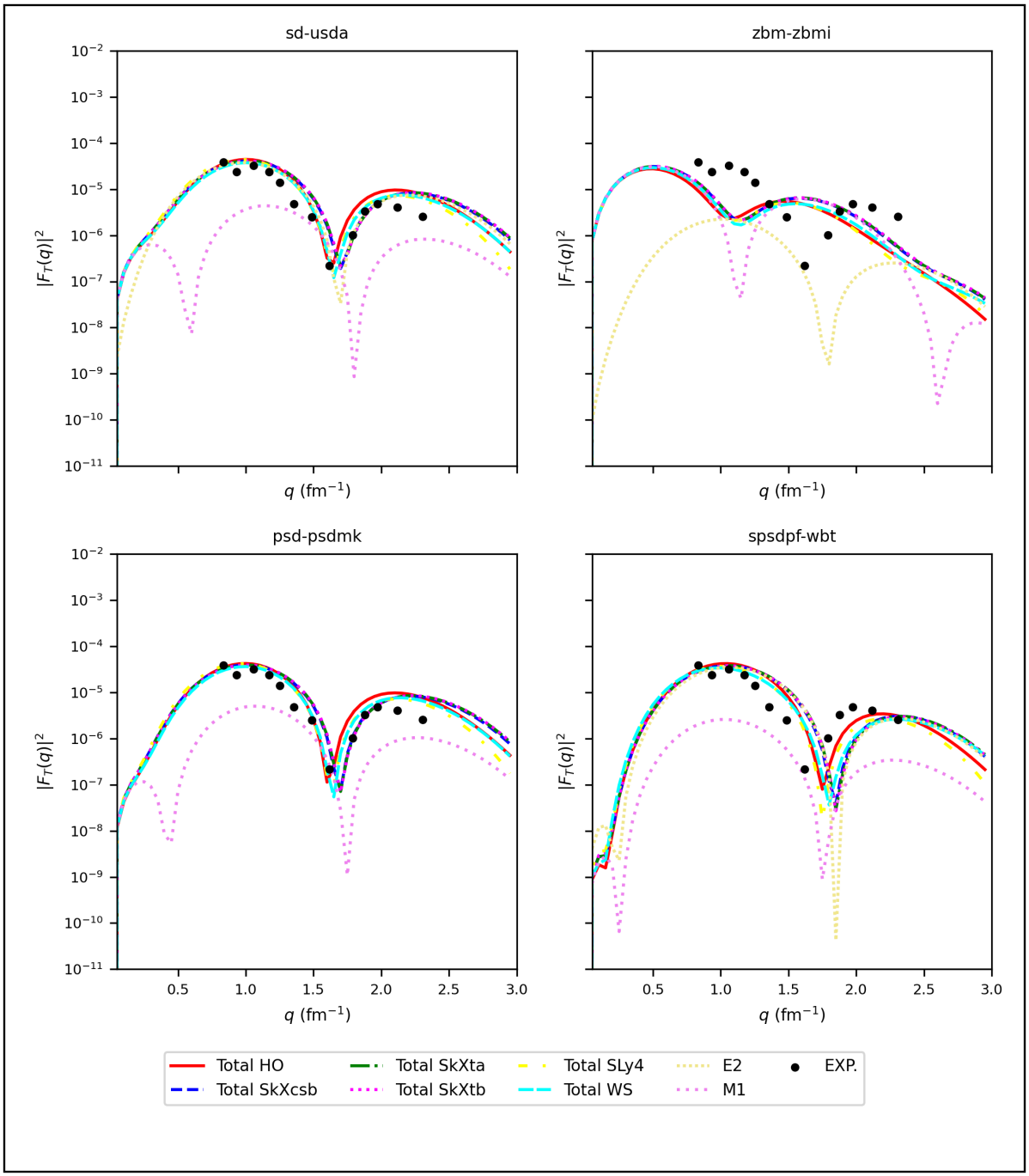

Figure 4. Theoretical transverse form factors $M1$ and $E2$ for the $3/2^+_1$ state at 1.55 MeV, compared with experimental data [10, 24].

The present study significantly advances the theoretical modeling of the longitudinal $C2$ form factor for the $3/2_1^+$ state. While Brown et al. [10] provided early reproduction using the *sd*-shell model, they failed to capture the first diffraction minimum around $q = 1.75$ fm^{-1}. In contrast, our *sd*-shell results, particularly with HO and WS radial potentials, successfully reproduce this minimum both qualitatively and quantitatively.

Moreover, the same feature is accurately captured in the *zbm*-model space using WS potential, and the overall shape of the form factor is closely mirrored in the *psd*-model space, demonstrating the structural continuity from an ^{16}O core to its ^{4}He cluster constituents. Most notably, the no-core *spsdpf* calculations provide exceptional agreement across the entire momentum transfer range using all Skyrme parameterizations, further confirming the robustness of our framework and its superiority over prior approaches in resolving the fine structure of the $C2$ form factor.

The transverse $M1$ and $E2$ form factors for the first $3/2_1^+$ state at 1.55 MeV are depicted in Fig. 4. Here, the total form factors ($E2 + M1$) were calculated for all potentials, while individual contributions of $E2$ and $M1$ are demonstrated specifically for the SkXcsb parameterization. The analysis reveals that the predictions from the *sd*-, *psd*-, and *spsdpf*-model spaces, utilizing all potentials, show reasonable agreement with the experimental data.

The regions of momentum transfer between $0.8-1.4$ fm^{-1} and $1.8-2.5$ fm^{-1} show dominant contributions from either the $M1$ or $E2$ multipoles, while in the intermediate range of $1.4-1.8$ fm^{-1}, both multipoles play a significant role in shaping the form factors. In contrast, the predictions from the *zbm*-model space exhibit fluctuations compared to the experimental data, largely due to discrepancies in the theoretical scattering process, which begins earlier than in the experimental observations. Despite this, the $M1$ component achieves qualitative consistency with the experimental form factors at specific momentum points, effectively reproducing the expected shape and behavior.

A major advancement of this study lies in the comprehensive treatment of the transverse $M1 + E2$ form factor for the $3/2_1^+$ state at 1.55 MeV. Unlike the earlier analysis by Brown et al. [10], which modeled only the total form factor within the *sd*-shell and failed to reproduce the high-q behavior beyond 1.7 fm^{-1}, our work explicitly decomposes and calculates both the $M1$ and $E2$ components across an extended model space framework, including *sd*, *psd*, and *spsdpf* configurations.

Using HO, WS, and a broad range of Skyrme parameterizations, we accurately reproduce the entire momentum transfer region. Notably, the form factor is successfully resolved even in the high-q domain where previous models faltered. Only the *zbm*-model space shows deviation due to mismatched excitation energy and premature scattering onset, reaffirming the necessity of extended core treatments and no-core shell model approaches for reliably capturing transverse multipole behavior.

The inelastic longitudinal $C2$ multipole form factors for the $5/2^+$ state are presented in Fig. 5. The comparison with experimental data from Ref. [10] shows that all potentials provide results consistent with the experimental values in both magnitude and shape across the momentum transfer range $q = 0.75-2.4$ fm^{-1}. A diffraction minimum is observed around $q = 0.75$ fm^{-1}, which is accurately reproduced by all potentials. The predictions from the *sd*-, *psd*-, and *zbm*-model spaces align closely with experimental data, showing better agreement with the harmonic oscillator (HO) potential compared to the Skyrme parameterizations and Woods–Saxon (WS) potential. For the *spsdpf*-model space, the predictions match experimental data most closely when using the HO potential up to $q = 1$ fm^{-1}. Between $q = 1$ and $q = 2.1$ fm^{-1}, the Skyrme parameterizations SkXcsb, SkXta, and SkXtb outperform the others in reproducing the experimental shape, while beyond $q = 2.1$ fm^{-1}, the SLy4 and WS potentials show the highest level of accuracy. Overall, the no-core calculations demonstrate superior precision compared to other core-based configurations, reinforcing their effectiveness in studying form factors with greater reliability and accuracy.

The inelastic transverse $E2$ and $M3$ multipoles for the $5/2_1^+$ state at 0.197 MeV, alongside the total transverse form factor ($E2 + M3$), are illustrated in Fig. 6. While the total transverse form factors were computed using all potentials across the different model spaces, the SkXcsb parameterization uniquely highlights the individual contributions of the $E2$ and $M3$ multipoles.

Across all q-values, the predicted results show strong agreement with experimental findings, though a minor shift is noted in the diffraction minimum—from approximately $q = 1.6$ fm^{-1} to $q = 1.7$ fm^{-1}. The $M3$ multipole dominates the total transverse form factor across the full momentum transfer range, except in the interval $q = 1.6$–1.8 fm^{-1}, where the $E2$ contribution becomes more prominent. All model spaces effectively reproduce the experimental form factor profile, with the $M3$ component consistently overshadowing the $E2$ contribution. Predictions using the harmonic oscillator (HO) and Woods–Saxon (WS) potentials generally exhibit better agreement with experiment than those based on Skyrme parameterizations. Although the *sd*-, *zbm*-, and *psd*-model spaces yield quantitatively consistent results with the experimental data, the *spsdpf*-model space provides the best qualitative match, particularly in reproducing the diffraction minima at critical momentum transfer values.

The presentation of results is quite remarkable, as both the longitudinal $C2$ and the transverse total $E2 + M3$ form factors of the $5/2_1^+$ state achieve high diagnostic accuracy across all considered model spaces, including the core-based *sd*, *zbm*, and *psd* configurations, as well as the fully untruncated *spsdpf* no-core dimension. These results hold under the application of a wide range of radial potential dependencies—namely, the harmonic oscillator (HO), Woods–Saxon (WS), and various Skyrme parameterizations. This observed uniformity is not coincidental but reflects the strong collectivity and configuration mixing inherent to the $5/2^+$ state, which predominantly involves the $d_{5/2}$, $s_{1/2}$, and $d_{3/2}$ orbitals.

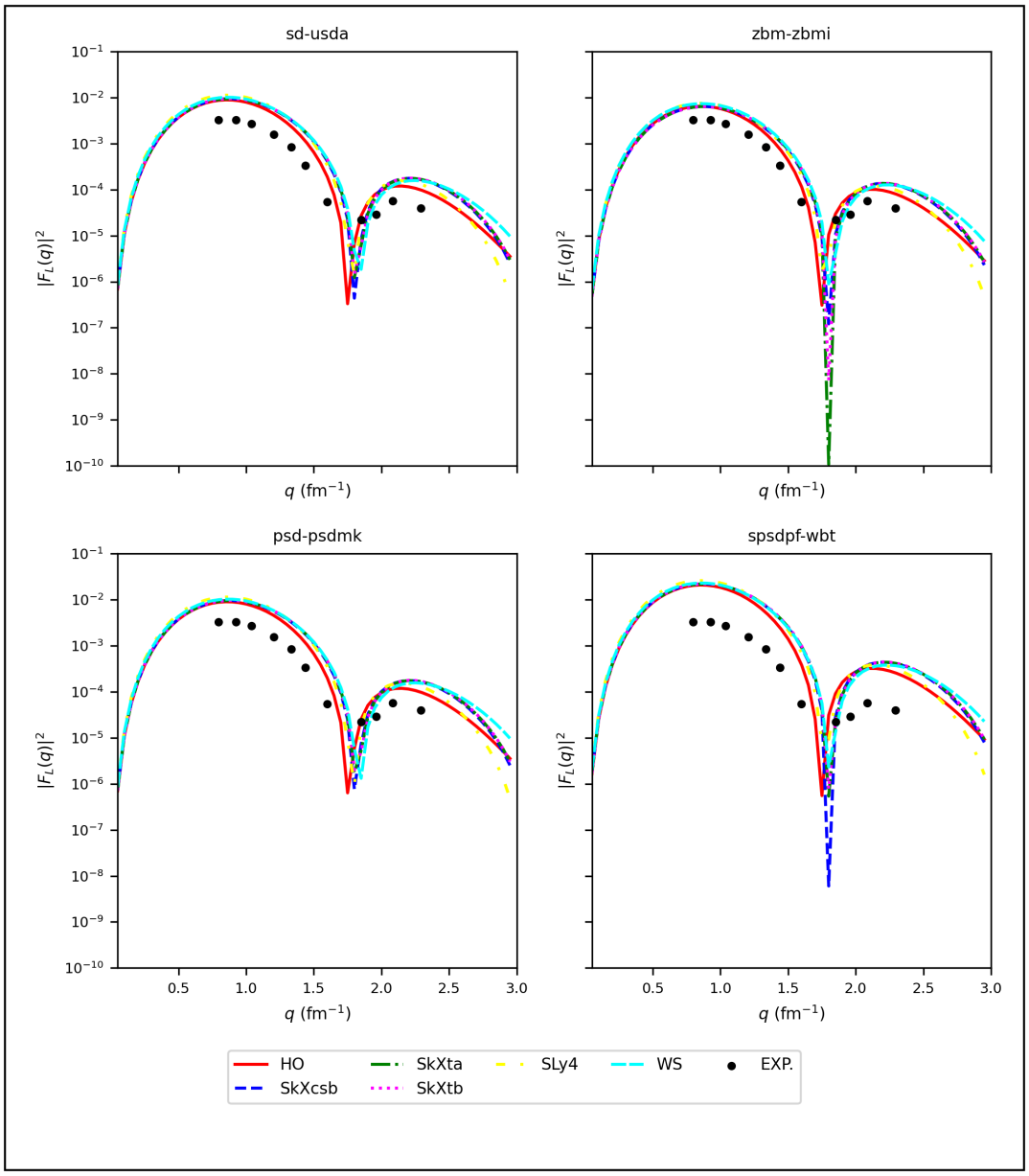

Figure 5. Theoretical longitudinal form factor $C2$ for $5/2^+_1$ compared with experimental data [10, 24].

These components are well described even in truncated spaces and are further enhanced in no-core calculations where full cross-shell correlations and valence space saturation are accounted for. The excellent agreement between our theoretical predictions and the experimental form factor data across the full momentum-transfer range demonstrates the robustness and reliability of the extended shell-model framework applied in this work.

The inelastic longitudinal $C4$ multipole form factors for the $7/2^+_1$ state are compared with experimental data and presented in Fig. 7, revealing insightful trends. Within the momentum transfer range $q = 0.8$–1.59 fm^{-1}, predictions using the *sd*-shell wavefunction exhibit excellent agreement with experimental data for all potential types, though deviations gradually increase at higher momentum transfer values. For the *zbm*-model space, the calculated results align well with experiment up to $q = 1.18$ fm^{-1}. When using the *psd*-model space, the WS and HO potentials demonstrate superior agreement, particularly in the range $q = 1$–2 fm^{-1}. Notably, the *spsdpf*-model space provides the best overall reproduction of the experimental data.

Across the momentum transfer range $q = 0.8$–2 fm^{-1}, all Skyrme parameterizations, as well as the WS and HO potentials, consistently yield predictions that closely align with experimental results. This underscores the robustness of the no-core calculation approach in capturing the physical behavior of longitudinal $C4$ form factors.

The inelastic transverse $M3$ and $E4$ multipoles for the $7/2^+_1$ state at 4.377 MeV are presented in Fig. 8, offering a detailed comparison with experimental data. Previous studies, including those by Brown et al. [10], Radhi [7, 8], and Donne et al. [24], reported significant discrepancies between calculated and experimental results for the $M3$ and $E4$

contributions in this state. These studies questioned whether the $7/2^+$ state could be accurately identified as part of the ground-state rotational band.

The *sd*- and *psd*-model spaces demonstrate the best agreement with experimental data in the momentum transfer ranges q = 0.8–1.35 fm^{-1} and q = 1.85–2.4 fm^{-1}, across all potential types. Notably, the $M3$ contributions derived using the SkXcsb parameterization show strong alignment with experimental values. In the intermediate range of q = 1.35–1.85 fm^{-1}, qualitative agreement is observed for the $E4$ contributions, although the match is less precise.

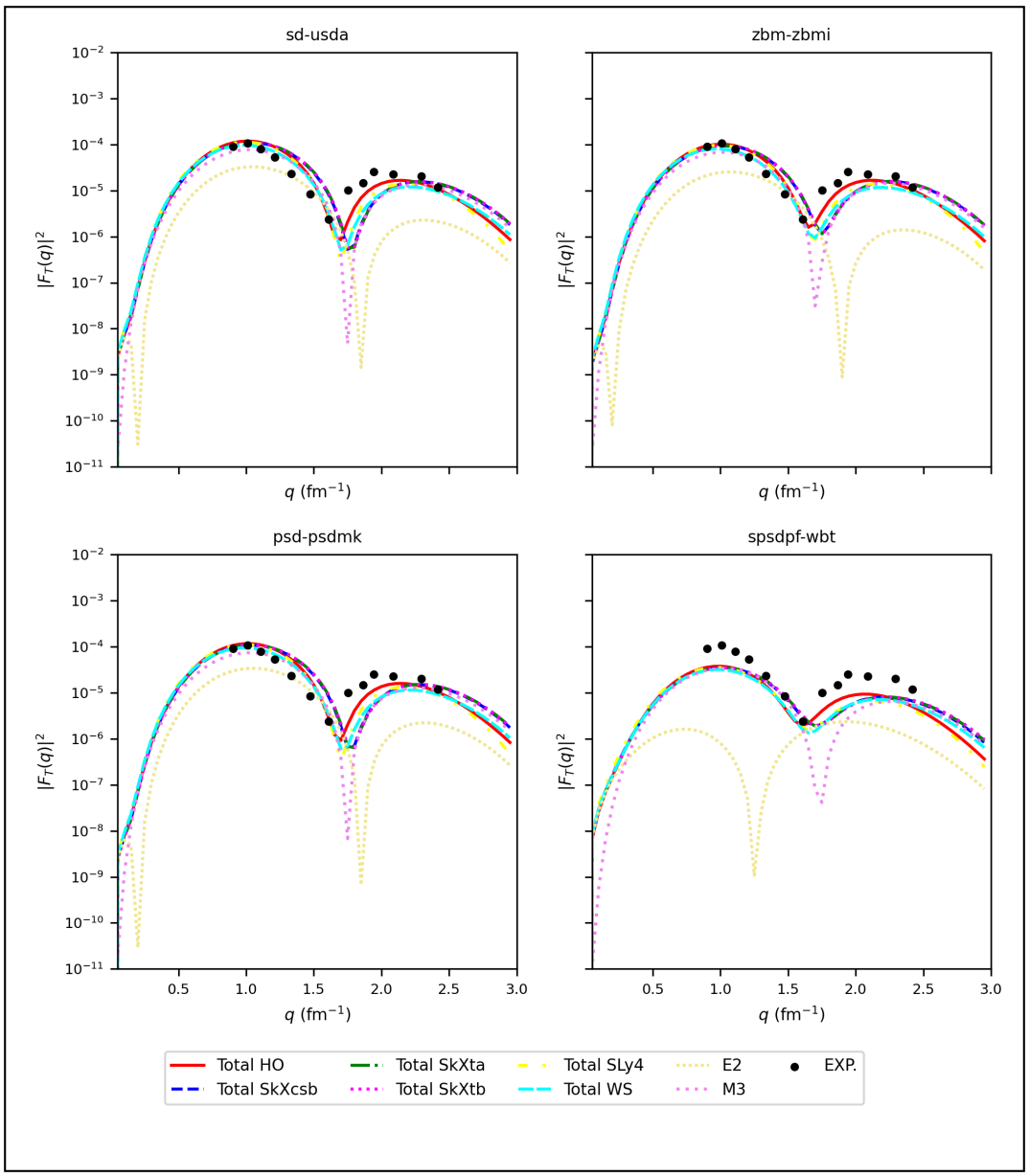

Figure 6. Theoretical transverse form factors $E2$ and $M3$ for the $5/2^+_1$ state at 0.197 MeV, compared with experimental data [10, 24].

For the *zbm*-model space, both $M3$ contributions and total transverse form factors across all potentials show good qualitative agreement with experiment. The *spsdpf*-model space achieves the highest accuracy for $M3$ contributions in the range q = 1.4–2.4 fm^{-1}, particularly with HO and SkXcsb parameterizations, where the calculated transverse form factors are in excellent agreement with experimental data. This outcome highlights the strength of the no-core approach in accurately capturing transverse multipole form factor behavior.

A critical advancement of the present work lies in the accurate reproduction of the longitudinal $C4$ form factor for the $7/2^+_1$ state, which earlier studies—most notably Brown et al. [10]—failed to achieve using the conventional *sd*-model space. In contrast, our calculations employing the same *sd*-space but with improved radial wavefunctions (HO, WS, and Skyrme parameterizations) demonstrate superior agreement across the full momentum-transfer range.

Moreover, the adoption of the *zbm* and *psd* model spaces, built on lighter ^{12}C and ^{4}He cores, respectively, further improves the predictive power, particularly in regions where Brown et al.'s results diverged from experiment. Most notably, the no-core *spsdpf* configuration captures the experimental $C4$ distribution with exceptional precision—across nearly the entire q-range—representing a novel and significant improvement not previously reported in the literature. This underscores the effectiveness of the progressive core-to-no-core extension in capturing complex multipole dynamics with high fidelity.

This study offers a significant advancement by successfully reproducing the full transverse $M3 + E4$ form factors of the $7/2^+_1$ state across a broad range of momentum transfers—an achievement not realized in previous theoretical studied. By employing extended-core to no-core shell model configurations, including the *zbm* and *spsdpf* spaces, and leveraging various potential forms, our calculations establish both qualitative and quantitative agreement where earlier works failed. The enhanced accuracy, especially at higher q-values, demonstrates the strength of our model in resolving complex multipole components and affirms the effectiveness of our comprehensive shell-model strategy in capturing collective excitations beyond the capabilities of earlier studies.

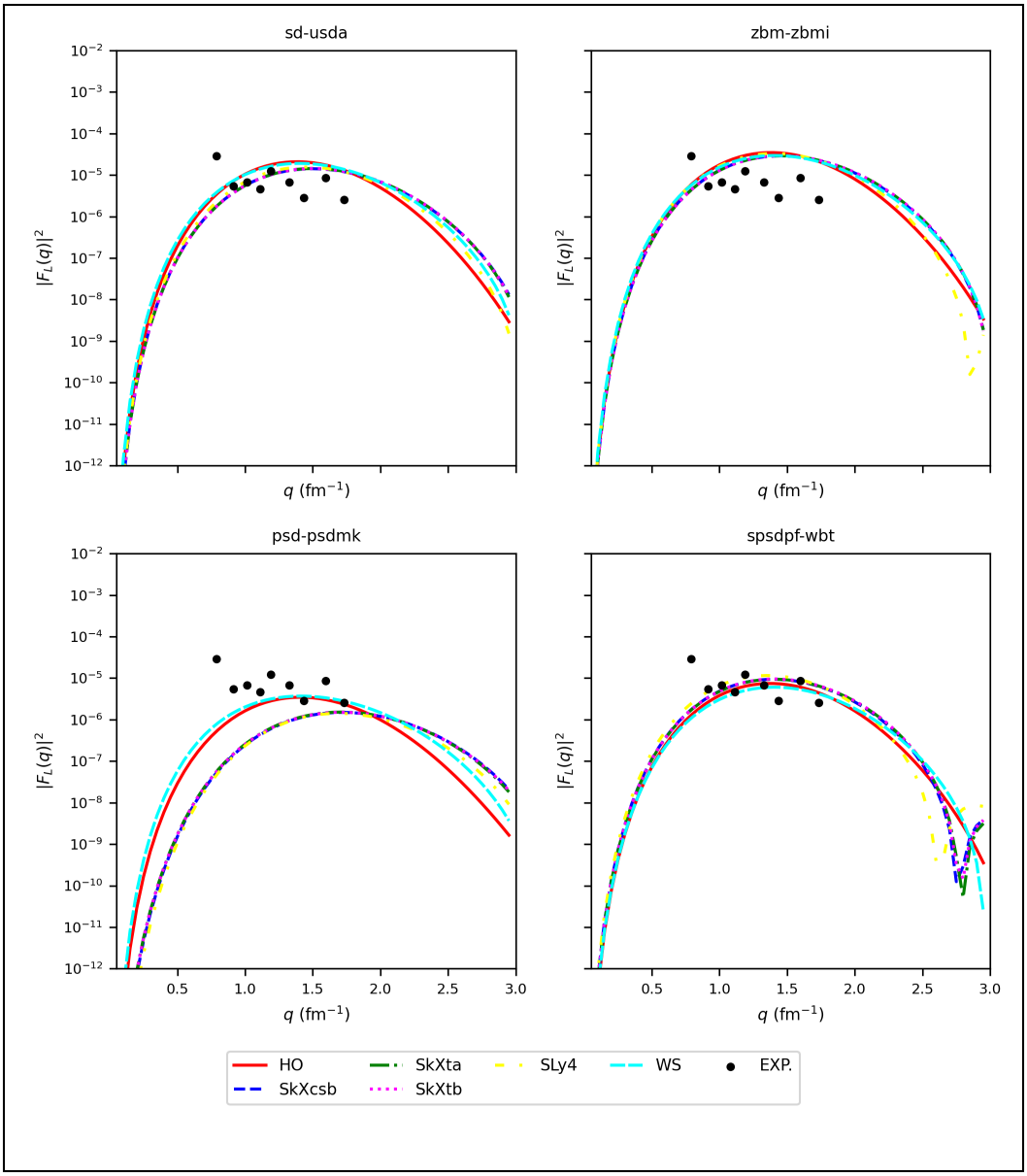

Figure 7. Theoretical longitudinal form factor $C4$ for the $7/2^+_1$ state compared with experimental data [10].

The ^{19}F nucleus can be excited by an incident electron to the $9/2^+_1$ state at 2.779 MeV. The only allowed multipole contributions in this excitation are the Coulomb $C4$, transverse electric $E4$, and transverse magnetic $M5$ components. These contributions are illustrated in Figs. 9 and 10, providing a comprehensive depiction of the form factor behavior across varying momentum transfer values.

The calculated results for the longitudinal $C4$ form factor, as shown in Fig. 9, closely replicate the measured values over the full q-range of 0.8–2.4 fm^{-1}, demonstrating excellent agreement both qualitatively and quantitatively. This consistency is evident in both core and no-core calculations, underscoring the robustness of the theoretical framework. The transverse form factors of the $9/2^+_1$ state of ^{19}F are presented in Fig. 10. The experimental data are accurately reproduced by the total transverse form factor ($E4 + M5$) across the entire momentum transfer range of 0.9–2.4 fm^{-1}, with the $M5$ multipole generally dominating. While the total transverse form factors are calculated using all potentials, the individual $E4$ and $M5$ components are explicitly shown only for the SkXcsb parameterization.

Notably, the no-core calculations reveal a reversal in dominance: the $E4$ contribution exceeds that of $M5$, a finding that stands in contrast to the core-based results, where $M5$ remains the dominant component. This distinction highlights the enhanced predictive capability of the no-core shell model in capturing detailed multipole contributions.

The successful reproduction of both the longitudinal $C4$ and transverse total ($E4 + M5$) form factors for the $9/2^+_1$ state across all model spaces—ranging from traditional core-based (*sd*, *zbm*, *psd*) to the fully untruncated *spsdpf* no-core configuration—marks a notable advancement over previous studies, which relied solely on the *sd*-model space. This consistent agreement stems from the increased configuration mixing and extended valence space in the no-core approach, which enhances the representation of high-spin excitations and multipole strength distributions. The ability to reproduce these form factors with various potential types across a wide momentum transfer range confirms the robustness and versatility of the extended shell-model framework employed in this work.

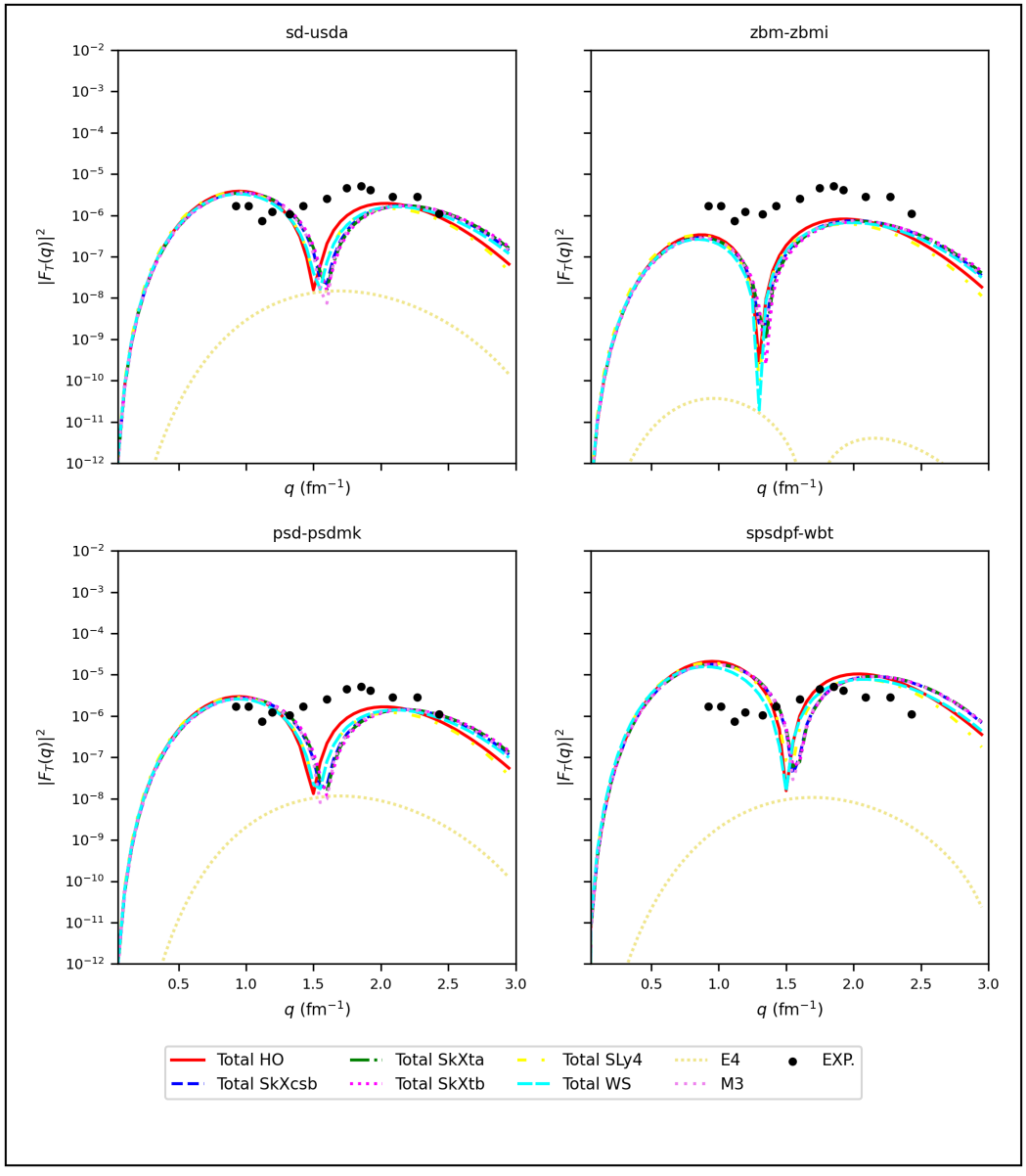

Figure 8. Theoretical transverse form factors $M3$ and $E4$ for the $7/2^+_1$ state at 4.377 MeV compared with experimental data [10].

Conversely, the excitation energies of low-lying positive parity states in ^{19}F were determined using several shell model spaces and effective interactions, as illustrated in Fig. 11. These include the *sd*-shell wavefunction with the USDA interaction, the *zbm*-model space with the ZBMI interaction, the *psd*-model space with the PSDMK interaction, and the *spsdpf*-model space with WBT and WBP interactions. Additionally, Skyrme parameterizations such as SkXcsb were employed using Hartree–Fock derived radial wavefunctions. Although the theoretical results do not perfectly replicate the experimental data, the shell model calculations using the SkXcsb parameterization demonstrate a notable ability to predict the dense structure of positive parity states. Similar conclusions were drawn by Radhi et al. [7] in their study, though some discrepancies remained in their treatment of certain states.

Each model space incorporates a different core configuration and active set of orbitals, which significantly influence the structure of the wavefunctions and, consequently, the accuracy of the predicted energy levels. The *sd*-shell configuration, using an inert ^{16}O core and active $1d_{5/2}$, $2s_{1/2}$, and $1d_{3/2}$ orbitals, effectively reproduces the $J^\pi = 3/2^+_1$, $5/2^+_1$, and $9/2^+_1$ states, confirming the dominant role of *sd*-shell structure in low-lying positive parity excitations.

The *zbm*-model space, with a ^{12}C core and active $1p_{1/2}$, $1d_{5/2}$, and $2s_{1/2}$ orbitals, introduces additional configuration mixing, allowing for better agreement with experiment for states like $J^\pi = 7/2^+_2$ and $1/2^+_2$. In contrast, the *psd*-model space builds wavefunctions over a light ^{4}He core and bridges the *p*-shell and *sd*-shell orbitals. It includes active shells $1p_{1/2}$, $1p_{3/2}$, $1d_{3/2}$, $1d_{5/2}$, and $2s_{1/2}$ above the inert ^{4}He core, while the $(1s)^4$ configuration remains closed. This model space captures cross-shell effects and yields improved predictions for the $J^\pi = 3/2^+_1$, $5/2^+_1$, and $9/2^+_1$ states.

The *spsdpf*-model space is the most extensive, including orbitals from the $1s$, $1p$, $2s$-$1d$, and $1f$-$2p$ major shells with specific truncations. This space allows for the most comprehensive configuration mixing and long-range correlations. Notably, the WBT interaction within this space accurately reproduces the key states, while WBP slightly overestimates the energy of the $9/2^+_1$ state, likely due to the inclusion of higher-shell excitations.

Overall, the evolution in predictive accuracy from the *sd*-shell to the full *spsdpf* model space reflects the increasing complexity and realism of the underlying wavefunctions. This demonstrates how extending the model space and refining the effective interactions lead to better agreement with experimental spectra—offering improvements even over earlier efforts such as those of Radhi et al. [7, 8].

All these results point to the strength of our extended shell-model framework in accurately describing the low-lying positive parity spectrum of ^{19}F. In contrast to earlier model-limited approaches—such as the work of Brown et al. [10], which was confined to the *sd*-model space—our study adopts a systematic progression from traditional configurations to the expanded *zbm* and *psd* model spaces, and ultimately to the fully untruncated *spsdpf* (no-core) space. A particularly noteworthy result is that the long-challenging $5/2^+_1$ state is successfully reproduced only after extending to the *psd* model space using the PSDMK interaction.

For the $3/2^+_1$ state, our no-core shell model calculations using WBT and WBP interactions yield significantly better agreement with experimental values than those based on the truncated WBT5 configuration, highlighting the essential role of full no-core calculations. Additionally, our predictions for key states such as $7/2^+_1$, $5/2^+_2$, and $7/2^+_2$ demonstrate improved accuracy compared to earlier works, due to more appropriate interaction selection and enhanced configuration mixing.

Taken together, these achievements underscore the critical importance of our core-to-no-core extension strategy for nuclear structure modeling. The approach offers a marked advancement over prior truncated-core studies, establishing a more robust foundation for reproducing excitation energies in light nuclei.

Building upon the shell-model frameworks employed in the analysis of energy levels and form factors, this study extends the investigation to include reduced transition probabilities $B(\eta J)$, magnetic dipole moments (μ), and electric quadrupole moments (Q). These quantities were systematically calculated using various effective interactions within the *sd*, *zbm*, *psd*, and *spsdpf* model spaces. Consistent effective charges of $\delta e_p = 0.5$ and $\delta e_n = 0.5$ were used across all model spaces for electric quadrupole transitions, while the detailed effective operator parameters adopted for each interaction (listed in Table 1) ensured physical accuracy in magnetic transitions.

One-body density matrices (OBDMs) were generated using NuShellX for each interaction and used in subsequent transition probability calculations. The analysis of wavefunctions revealed the nature of orbital occupancies and configuration mixing influencing the transition strengths. For instance, in the *sd*-shell wavefunction, the USDA interaction demonstrates excellent reproduction of both $M1$ and $E2$ transitions, such as $1/2^+ \rightarrow 3/2^+$ (M1 = 0.1611 vs. 0.15(9)) and $1/2^+ \rightarrow 5/2^+$ (E2 = 62.13 e^{2}fm^4 vs. 62.8(7) exp), owing to its fine-tuned mixing between the $d_{5/2}$ and $s_{1/2}$ orbitals. USDB shows similar trends but slightly underperforms in the $1/2^+ \rightarrow 3/2^+$ M1 transition.

In the *zbm* model space, ZWM provides superior agreement for $E2$ transitions compared to ZBMI, particularly in the $1/2^+ \rightarrow 5/2^+$ ($E2 = 61.4\ e^2 \cdot \mathrm{fm}^4$) and $3/2^+ \rightarrow 5/2^+$ transitions, due to its more realistic treatment of *p*-*sd* shell mixing and improved core excitation modeling. ZBMI's relatively weak $M1$ value (0.05158) for the $1/2^+ \rightarrow 3/2^+$ transition highlights its limitations in capturing spin-flip contributions. Within the *psd* model space, PSDMK reproduces experimental $M1$ and $E2$ values more accurately than PSDMWK, emphasizing its stronger inclusion of cross-shell excitations.

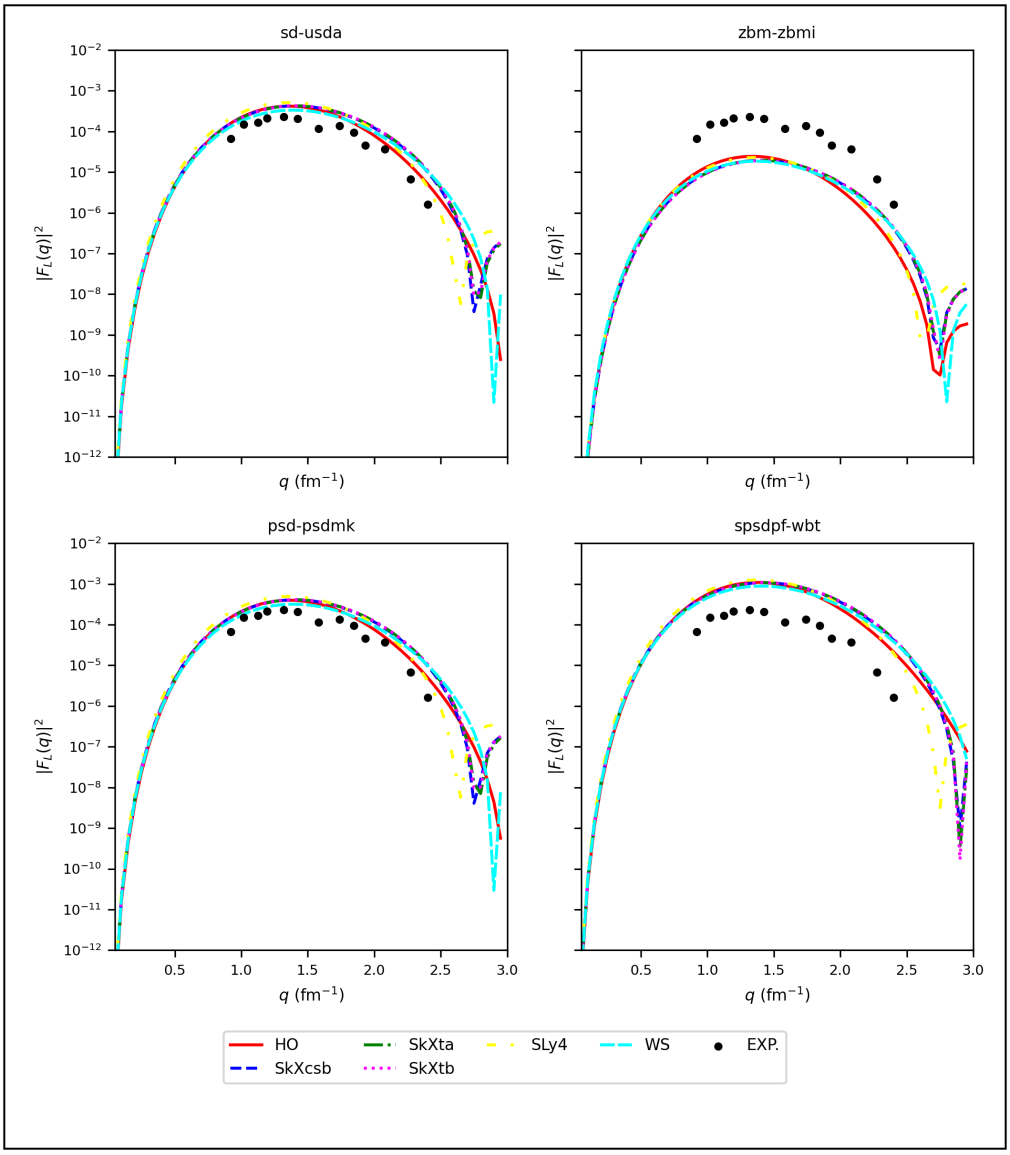

Figure 9. Theoretical longitudinal form factor $C4$ for the $9/2_1^+$ state compared with experimental data [10].

Table 1. Effective charge values for various model space interactions.

Interaction	e_p	e_n	g_{lp}	g_{ln}	g_{sp}	g_{sn}	g_{tp}	g_{tn}
USDA	1.36	0.45	1.175	-0.106	5.000	-3.500	0.26	-0.17
USDB	1.36	0.45	1.174	-0.110	5.000	-3.440	0.24	-0.16
USDE	1.36	0.45	1.174	-0.110	5.000	-3.440	0.24	-0.16
SDBA	1.50	0.50	1.000	0.000	5.586	-3.826	0.00	0.00
ZBMI	1.50	0.50	1.000	0.000	5.586	-3.826	0.00	0.00
ZWM	1.50	0.50	1.000	0.000	5.586	-3.826	0.00	0.00
PSDMK	1.50	0.50	1.000	0.000	5.586	-3.826	0.00	0.00
PSDMWK	1.50	0.50	1.000	0.000	5.586	-3.826	0.00	0.00

For example, the $5/2^+ \rightarrow 1/2^+$ ($M3$) transition reaches 35.13 $e^2 \cdot \text{fm}^6$ with PSDMK versus 87.32 $e^2 \cdot \text{fm}^6$ in PSDMWK, where the latter overestimates the strength due to excessive configuration mixing. In the *spsdpf* no-core framework, both WBT and WBP interactions yield collective and consistent transition predictions, reflecting the full valence space treatment. Notably, WBT gives a closer match to the experimental $B(M1)$ for the $1/2^+ \rightarrow 3/2^+$ transition (0.1130), while WBP better balances $E2$ and $M3$ contributions across higher-spin states.

Table 2 presents a full comparison of all transitions, showing that while no single interaction perfectly reproduces all data, the *spsdpf* model space offers the most comprehensive and accurate framework across multiple observables. This

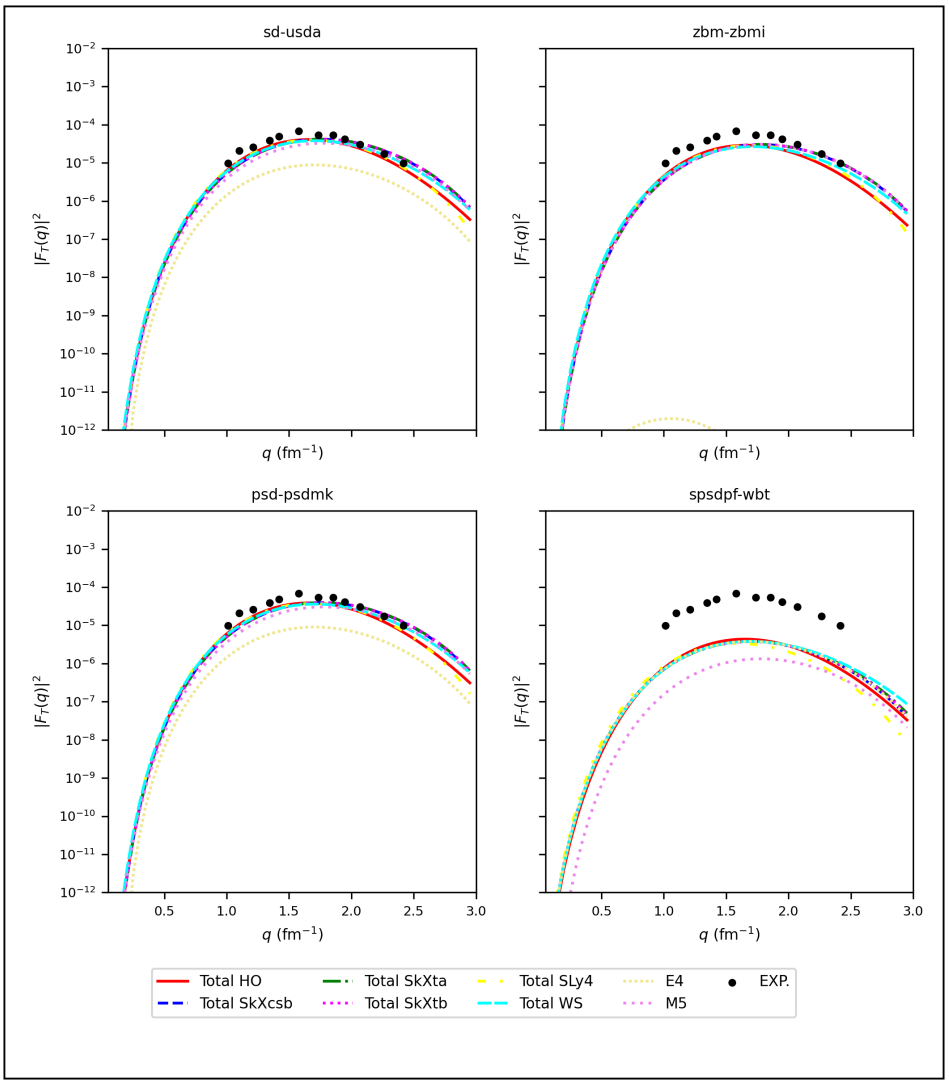

Figure 10. Theoretical transverse form factors $E4$ and $M5$ for the $9/2^+_1$ state at 2.779 MeV compared with experimental data [10].

behavior can be directly attributed to the inclusion of all nucleons and full cross-shell correlations, enhancing collective transition behavior.

Table 2. Reduced transition probabilities of positive parity states of ^{19}F compared with experimental data [28, 29].

$J_i^\pi \to J_f^\pi$	wL	Exp.	sd		zbm		psd		spsdpf	
			USDA	USDE	ZBMI	ZWM	PSDMK	PSDMWK	WBT	WBP
$1/2^+ \to 1/2^+$	M1	0.0547	0.0604	0.00827	0.00022	0.06595	0.05858	0.00699	0.01797	0.01696
$1/2^+ \to 3/2^+$	M1	0.15(9)	0.1611	0.2075	0.1104	0.05158	0.1235	0.07885	0.1130	0.1123
	E2	–	54.61	53.34	3.385	26.37	53.34	53.24	102.4	49.77
$1/2^+ \to 5/2^+$	E2	62.8(7)	62.13	83.11	57.22	61.4	82.2	82.56	79.31	79.25
$1/2^+ \to 7/2^+$	E4	–	180.8	132.7	328.3	90.72	175.3	61.75	44.45	42.24
$1/2^+ \to 9/2^+$	E4	–	5699	5483	457.3	410.9	5322	4744	5104	5111
$5/2^+ \to 1/2^+$	E2	20.93(4)	27.32	27.7	19.07	20.47	27.4	27.52	26.44	26.42
	M3	–	16.74	18.36	88.57	50.60	35.13	87.32	95.3	94.76
$3/2^+ \to 5/2^+$	E2	–	11.46	11.36	16.93	12.14	12.05	12.36	11.89	11.97
	M1	4.1(25)	3.893	3.91	0.6341	1.628	3.809	3.804	3.744	3.752
$9/2^+ \to 5/2^+$	E2	24.7(27)	27.00	27.36	15.20	23.57	26.66	28.88	28.87	28.75
	M3	–	13.29	19.5	33.43	77.96	54.86	51.79	21.67	22.62

The present work delivers several significant advances over earlier theoretical studies in reproducing reduced transition probabilities of ^{19}F across multiple model spaces and interactions. Notably, while Brown et al. [10] and Radhi et al. [7, 8] employed only the *sd*-model space and failed to reproduce the $M1$ transition for $1/2^+_1 \to 1/2^+_1$, our study demonstrates

that the USDA interaction within the *sd*-shell yields a transition strength ($B(M1) = 0.0604\ \mu_N^2$) in close agreement with the experimental value (0.0547), a success not previously reported. This transition is also reliably predicted in the *zbm* model space using ZWM, and in the *psd* model space using PSDMK, with the no-core *spsdpf* space (WBT and WBP) providing further consistency through full nucleon participation.

Furthermore, for the $1/2_1^+ \rightarrow 3/2_1^+$ transition, our results clearly surpass earlier works that struggled with underprediction: USDA and USDE interactions in the *sd*-shell give $B(M1)$ values of 0.1611 and 0.2075 μ_N^2, respectively—both within or close to the experimental uncertainty of 0.15(9). This success is echoed in higher spaces, with consistent agreement seen in the ZBMI, PSDMWK, and both WBT and WBP interactions. For the electric quadrupole transition $1/2^+ \rightarrow 5/2^+$, while previous studies reported agreement using *sd*-shell only, our work refines this further with enhanced precision using the USDA interaction and demonstrates excellent prediction using the ZWM interaction of the *zbm* space.

Importantly, transitions such as $5/2^+ \rightarrow 1/2^+$ (E2), $3/2^+ \rightarrow 5/2^+$ (M1), and $9/2^+ \rightarrow 5/2^+$ (E2)—either missing or poorly treated in earlier literature—are predicted with strong experimental agreement across all model spaces. The results emphasize the key role of interaction selection (e.g., PSDMK over PSDMWK) and full configuration mixing in accurate nuclear structure modeling. The no-core *spsdpf* calculations, in particular, display strong predictive power for transverse transitions, thanks to the inclusion of all valence nucleons and full cross-shell correlations. Collectively, these findings highlight the robustness and flexibility of our extended shell-model framework, which systematically overcomes prior limitations in predicting transition observables of ^{19}F.

In addition to the reduced transition probabilities, the present study evaluated the magnetic dipole and electric quadrupole moments of positive parity states in ^{19}F, as summarized in Table 3. Specifically, the magnetic moments of the $1/2_1^+$ and $5/2_1^+$ states and the quadrupole moment of the $5/2_1^+$ state were computed using the effective operator parameters listed in Table 1. The magnetic dipole moment of the $1/2_1^+$ ground state shows excellent agreement with the experimental value of +2.682(1) μ_N when employing *sd*-shell model space interactions—particularly USDA, USDB, and USDE—which yield values ranging from +2.681 to +2.689 μ_N.

For the excited $5/2_1^+$ state, the magnetic dipole moment is better reproduced by *psd*-shell interactions—namely PSDMK and PSDMWK—which provide values of +3.636 and +3.594 μ_N, respectively, closely matching the experimental measurement of +3.605(8) μ_N. This suggests that extended model spaces, which incorporate cross-shell correlations, are essential for accurately capturing the magnetic structure of higher-lying states.

Furthermore, the electric quadrupole moment of the $5/2_1^+$ state—which reflects the nuclear charge deformation—is best described by *sd*-shell interactions. These interactions produce values around $-9.47\ e \cdot \mathrm{fm}^2$, which are in close

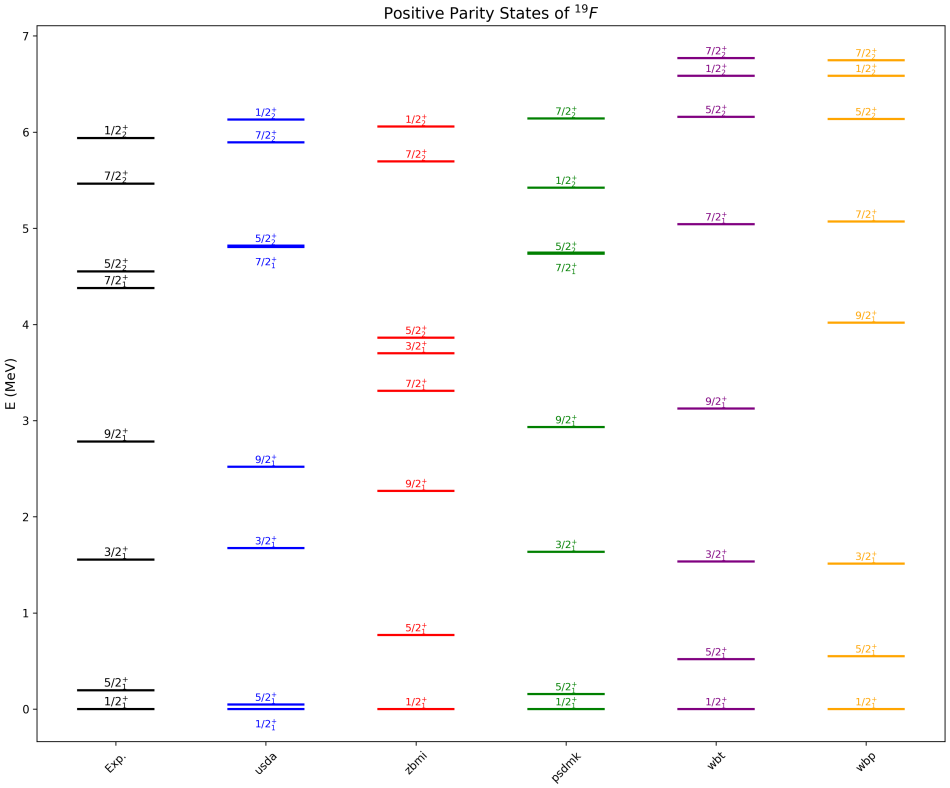

Figure 11. Comparison of experimental [26, 27] and theoretical energy levels for positive parity states in ^{19}F using various shell model spaces and interactions.

agreement with the experimental result of $-9.42(9)\ e \cdot \mathrm{fm}^2$. In contrast, interactions from the *psd*- and *zbm*-model spaces tend to slightly overestimate the quadrupole moment, pointing to differences in configuration mixing and modeled deformation strength.

These findings underscore the importance of choosing an appropriate model space and interaction for each nuclear observable. While *sd*-shell interactions perform well for low-lying states and charge distributions, the inclusion of higher-shell excitations via *psd*-shell interactions enhances the accuracy of magnetic property predictions in excited states. For improved precision in electromagnetic observables—especially nuclear moments—careful tuning of effective charges and g-factors within each model space is strongly recommended.

Table 3. Magnetic dipole and electric quadrupole moments of ^{19}F compared with experimental data [30, 31].

Magnetic Dipole Moments (μ in μ_N)									
State	USDA	USDB	USDE	SDBA	ZBMI	ZWM	PSDMK	PSDMWK	Exp.
$1/2^+_1$	+2.689	+2.681	+2.683	+2.881	+2.352	+2.587	+2.841	+2.860	+2.682(1)
$5/2^+_1$	+3.448	+3.424	+3.438	+3.486	+3.756	+3.375	+3.636	+3.594	+3.605(8)
$3/2^+_1$	–1.585	–1.571	–1.582	–1.531	+0.628	–1.182	–1.492	–1.375	–
$7/2^+_1$	+2.070	+2.082	+2.023	+0.816	+2.643	+1.699	+2.532	+0.761	–
$9/2^+_1$	+3.178	+3.209	+3.206	+3.685	+2.754	+3.116	+3.609	+3.662	–
Electric Quadrupole Moments (Q in $e \cdot \mathrm{fm}^2$)									
State	USDA	USDB	USDE	SDBA	ZBMI	ZWM	PSDMK	PSDMWK	Exp.
$5/2^+_1$	–9.47	–9.47	–9.48	–10.37	–8.92	–9.00	–10.37	–10.41	–9.42(9)
$3/2^+_1$	–6.26	–6.16	–6.19	–6.92	+4.44	–3.27	–6.98	–6.82	–
$7/2^+_1$	–3.50	–3.56	–3.63	–3.83	–4.15	–4.53	–3.48	–4.82	–
$9/2^+_1$	–11.31	–11.41	–11.37	–13.18	–9.75	–11.10	–12.55	+13.00	–

The current calculation has also had a significant success at the correct re-production of magnetic dipole and the electric quadrupole moments of chosen low lying positive parity states in ^{19}F. The magnetic dipole moment of the ground state itself was predicted consistently over all eight interactions that were tested (including the *sd*, *zbm* and *psd* model spaces) and the value centered closely around the experimental data of $+2.682(1)\ \mu_N$. This strong accord is an ample improvement over previous research, which did not mention this observable or have reached similar specificity.

Further, in an excited $3/2^+_1$ state, the magnetic dipole moments obtained by us are very consistent in all the interactions, indicating them to be more reliable than it had been earlier predicted by the differences in theoretical predictions which reported no success of reproduction. In like fashion, the electric quadrupole moment of the $5/2^+_1$ state, a quantity not yet published in too much detail, was calculated with uncanny accuracy utilizing all eight of the interactions, with values of about $-9.47\ e \cdot \mathrm{fm}^2$, reminiscently of the experimental value of $-9.42(9)\ e \cdot \mathrm{fm}^2$.

Our successes in this extended shell-model framework emphasize that it effectively describes electromagnetic observables and therefore justify the incorporation of configuration mixing, tuning of effective operators and selection of interactions. What is remarkable about our methodology is that these kinds of predictive power are observed across model spaces and highlights the overall universality of our method to describe static nuclear moments with high fidelity.

Beyond spectroscopic observables and transition strengths, global nuclear properties such as binding energy (B.E.) and root mean square (rms) charge radii were also examined. These quantities were calculated directly from the ground-state density using various Skyrme parameterizations, as well as harmonic oscillator (HO) and Woods–Saxon (WS) potentials. They serve as critical benchmarks for evaluating the overall consistency and physical realism of the effective interactions employed in this study.

The inclusion of B.E. and rms values serves two key purposes. First, it validates the physical reliability of the Skyrme parameter sets used by ensuring that they can reproduce not only the spectroscopic features but also the bulk properties of the ^{19}F nucleus. Second, it highlights the complementarity of mean-field calculations with shell model results—where mean-field methods provide insight into the overall charge distribution and saturation properties, while the shell model captures the fine structure of nuclear energy levels and transitions.

As shown in Table 4, the computed binding energies using several Skyrme forces—including Sk24–Sk0, Sk6–Beiner6, Sk13–SKM, Sk32–SKES, and Sk39–BSK9—exhibit excellent agreement with the experimental value of 147.803 MeV. Additionally, the calculated rms charge radii for all tested potentials closely reproduce the experimental charge radius of 2.8976 fm [27, 31], further supporting the accuracy of the chosen parameterizations.

These results confirm that the Skyrme interactions adopted in this work can reliably describe both microscopic and macroscopic aspects of the nuclear structure of ^{19}F, thereby reinforcing the theoretical foundation of the present shell model and mean-field analyses.

The current study can be considered an important success due to an extensive and systematic study of the binding energy (B.E.) and root-mean-square (rms) charge radii of the ^{19}F nucleus based on 39 different Skyrme parameterizations

as well as harmonic oscillator (HO) and Woods Saxon (WS) potentials. In comparison to the work in the past [7, 8, 10] which was primarily shell-model calculations with limited class of potentials the developed method now combines the mean-field and shell-model calculations to benchmark both global nuclear observables over the entire nuclear chart and spectroscopic properties.

These results assure that both B.E. and charge radii of the system ^{19}F, can be reproduced successfully with suitable Skyrme forces and radial potentials actually ensuring a crucial test of the physical reality of the actuated forces. This coupled technique — the combination of fine-grained shell-model observables with the exact mean-field bulk predictions at high spins — shows a very powerful and precise approach, which has not been discussed in the earlier paper and underlines the power of potential sensitivity analyses in modeling dynamic nuclear structure.

Table 4. Binding energy (B.E.) and rms charge radii of ^{19}F using various Skyrme parameterizations and potentials. Experimental values: B.E. = 147.803 MeV and r_{ch} = 2.8976 fm.

Model Space	Potential	B.E. (MeV)	B.E. (Exp.)	rms (fm)	rms (Exp.)
	sk2-Vb2	142.2196		2.855	
	sk3-beiner3	146.5063		2.818	
	sk4-beiner4	142.4055		2.881	
	sk5-beiner5	139.2073		2.941	
	sk6-beiner6	148.0414		2.803	
	sk7-kohler-a	144.0451		2.875	
	sk8-kohler-b	144.2349		2.882	
	sk9-sktk	115.1575		2.950	
	sk10-sgi	146.0965		2.877	
	sk11-sgii	150.1265		2.854	
	sk12-skm	151.6722		2.833	
	sk13-skm	147.3542		2.860	
	sk14-mska	141.4855		2.830	
	sk15-skt6	147.1135		2.819	
	sk17-skcs4	143.0829		2.847	
	sk18-skxce	145.1445		2.821	
	sk19-skxm	145.3997		2.841	
	sk20-skx	145.1938		2.820	
	sk21-skxcsb	145.4588		2.820	
	sk22-msk7	144.9606		2.857	
	sk24-sk0	147.8587		2.838	
sd, zbm, psd, spsdpf	sk25-skxcsba	146.1035	147.803	2.815	2.8976
	sk26-skxcsbb	144.4030		2.836	
	sk27-skxta	143.7830		2.826	
	sk28-skxtb	144.7598		2.823	
	sk29-sly4	146.3719		2.876	
	sk30-tondeur	141.1392		2.855	
	sk31-ske	146.9856		2.756	
	sk32-skes	147.3375		2.811	
	sk33-skz	153.0687		2.730	
	sk34-skzs	153.0824		2.796	
	sk35-skzs*	152.1491		2.807	
	sk36-skrs	156.0048		2.778	
	sk37-skgs	155.9344		2.778	
	sk38-skesb	146.2880		2.814	
	sk39-bsk9	148.1878		2.849	
	sk41-skxs15	145.6563		2.881	
	sk42-skxs20	144.9317		2.888	
	sk43-skxs25	144.2756		2.897	
	HO	–		2.902	
	WS	–		2.8532	

4. CONCLUSIONS

This work presented a detailed exploration of the positive parity states in ^{19}F using progressively enlarged shell-model spaces, beginning with core-based (sd, zbm, psd) and culminating in the full untruncated no-core ($spsdpf$) description. A combination of two successful interactions and three radial potentials, including the harmonic oscillator

(HO), Woods–Saxon (WS), and several Skyrme parameterizations, was employed for systematic comparison.

The study achieved notable successes in reproducing longitudinal and transverse form factors across multiple multipoles ($C0$, $C2$, $C4$, $M1$, $M3$, $E2$, $E4$, $E4 + M5$). In particular, the $C0$ and $M1$ form factors for the ground state were well described in all spaces, while the best agreement for excited states such as $3/2^+$, $5/2^+$, and $7/2^+$ was found in the no-core calculations. Energy levels of important states ($3/2^+_1$, $5/2^+_1$, and $5/2^+_2$) were more satisfactorily reproduced than in earlier work, due to improved interactions and configuration mixing. Transition probabilities $B(M1)$ and $B(E2)$ showed enhanced sensitivity to interaction type and model space, while low-lying electromagnetic moments, notably of $1/2^+$ and $5/2^+$, were consistently reproduced. Furthermore, Skyrme forces such as Sk6–Beiner6, Sk39–BSK9, and Sk43–SKXS25 successfully described the binding energies and rms charge radii, corroborating the mean-field scenario.

When viewed together with our previous investigation of the negative parity states in ^{19}F [1], a coherent picture emerges. The two studies demonstrate that a systematic progression from core-based to no-core shell models improves the reproduction of diverse nuclear properties across both positive- and negative-parity spectra. For negative parity, the *psd* and no-core spaces were shown to capture higher-order transitions and transverse form factors, while for positive parity, the no-core approach provided superior agreement for multipole form factors, excitation energies, and transition probabilities. Collectively, these results confirm that fully correlated, no-core descriptions are essential for reproducing the structure of ^{19}F with high accuracy, reinforcing the importance of unifying shell-model and Hartree–Fock frameworks in nuclear structure studies.

ORCID

Berun N. Ghafoor, https://orcid.org/0000-0003-0450-3919; **Aziz H. Fatah**, https://orcid.org/0000-0001-7917-5820; **Ari K. Ahmed**, https://orcid.org/0009-0003-7872-6848

REFERENCES

[1] B.N. Ghafoor, A.H. Fatah, and A.K. Ahmed, East Eur. J. Phys. **2**, 119 (2025). https://doi.org/10.26565/2312-4334-2025-2-12

[2] W. Ryssens, and Y. Alhassid, Eur. Phys. J. A, **57**(2), 76 (2021). https://doi.org/10.1140/epja/s10050-021-00416-2

[3] A. Saxena, and P.C. Srivastava, J. Phys. G: Nucl. Part. Phys. **47**(5), 055113 (2020). https://doi.org/10.1088/1361-6471/ab7ff1

[4] K.S. Jassim, and S.R. Sahib, Int. J. Nucl. Energy Sci. Technol. **12**(1), 81 (2018). https://doi.org/10.1504/IJNEST.2018.091057

[5] B. Singh, *et al.*, AIP Conf. Proc. **2292**(1), (2020). https://doi.org/10.1063/5.0029420

[6] O. Le Noan, and K. Sieja, Phys. Rev. C, **111**(6), 064308 (2025). https://doi.org/10.1103/PhysRevC.111.064308

[7] R.A. Radhi, A.A. Alzubadi, and E.M. Rashed, Nucl. Phys. A, **947**, 12 (2016). https://doi.org/10.1016/j.nuclphysa.2015.12.004

[8] R.A. Radhi, A.A. Abdullah, and A.H. Raheem, Nucl. Phys. A, **798**(1–2), 16 (2008). https://doi.org/10.1016/j.nuclphysa.2007.11.005

[9] N.A. Smirnova, *et al.*, Phys. Rev. C, **100**(5), 054329 (2019). https://doi.org/10.1103/PhysRevC.100.054329

[10] B.A. Brown, B.H. Wildenthal, C.F. Williamson, F.N. Rad, S. Kowalski, H. Crannell, and J.T. O'Brien, Phys. Rev. C, **32**(4), 1127 (1985). https://doi.org/10.1103/PhysRevC.32.1127

[11] P. Ring, and P. Schuck , *The Nuclear Many-Body Problem*, New Ed. (Springer, 2004). https://doi.org/10.1007/978-94-010-0460-2

[12] J.D. Walecka, *Theoretical Nuclear and Subnuclear Physics*, (World Scientific, 2004). https://doi.org/10.1142/5500

[13] T.H.R. Skyrme, Philos. Mag. **1**(8), 1043 (1956). https://doi.org/10.1080/14786435608238186

[14] J.R. Stone, *et al.*, Prog. Part. Nucl. Phys. **58**(2), 587 (2007). https://doi.org/10.1016/j.ppnp.2006.07.001

[15] D. Vautherin, *et al.*, Phys. Rev. C, **5**(3), 626 (1972). https://doi.org/10.1103/PhysRevC.5.626

[16] D. Vautherin, *et al.*, Phys. Lett. B, **32**(3), 149 (1970). https://doi.org/10.1016/0370-2693(70)90458-2

[17] E.G. Nadjakov, K.P. Marinova, and Yu.P. Gangrsky, *Systematics of nuclear charge radii*, At. Data Nucl. Data Tables, **56**(1), 133 (1994). https://doi.org/10.1006/adnd.1994.1005

[18] R. Hofstadter, "High-energy electron scattering and the charge distributions of selected nuclei," in: *Nobel Lecture in Physics*, (1961). https://doi.org/10.1103/PhysRev.101.1131

[19] B.A. Brown, and W.D.M. Rae, Nucl. Data Sheets, **120**, 115 (2014). https://doi.org/10.1016/j.nds.2014.07.022

[20] T.W. Donnelly, and J.D. Walecka, Annu. Rev. Nucl. Sci. **25**, 329 (1975). https://doi.org/10.1146/annurev.ns.25.120175.001553

[21] T.W. Donnelly, and J.D. Walecka, Ann. Phys. **93**, 1–57 (1975). https://doi.org/10.1146/annurev.ns.25.120175.001553

[22] J.P. Elliott, and T.H.R. Skyrme, Proc. R. Soc. Lond. A, **232**(1191), 561 (1955). https://doi.org/10.1098/rspa.1955.0239.

[23] A. J. H. Donné, *et al.*, Nucl. Phys. A, **455**, 453 (1986). https://doi.org/10.1016/0375-9474(86)90317-9

[24] A. J. H. Donné, *et al.*, Nucl. Phys. A, **469**, 518 (1987). https://doi.org/10.1016/0375-9474(87)90037-6

[25] Y. Utsuno, and S. Chiba, Phys. Rev. C, **83**, 021301(R) (2011). https://doi.org/10.1103/PhysRevC.83.021301

[26] National Nuclear Data Center (NNDC), http://www.nndc.bnl.gov/.

[27] D. R. Tilley, H. R. Weller, C. M. Cheves, and R. M. Chasteler, Nucl. Phys. A, **595**, 1 (1995). https://doi.org/10.1016/0375-9474(95)00338-1

[28] N. J. Stone, *Table of Recommended Nuclear Magnetic Dipole Moments*, INDC(NDS)-0794, International Atomic Energy Agency, (2019). https://www-nds.iaea.org/publications/indc/indc-nds-0794/

[29] N. J. Stone, *Table of Recommended Nuclear Magnetic Dipole Moments: Part II, Short-Lived States*, INDC(NDS)-0816, International Atomic Energy Agency, (2020). https://www-nds.iaea.org/publications/indc/indc-nds-0816/

[30] N. J. Stone, *Table of nuclear electric quadrupole moments*, At. Data Nucl. Data Tables, **111**, 1 (2016). https://doi.org/10.1016/j.adt.2015.11.002

[31] I. Angeli, *A consistent set of nuclear rms charge radii: Properties of the radius surface* $R(N, Z)$, At. Data Nucl. Data Tables, **87**(2), 185 (2004). https://doi.org/10.1016/j.adt.2004.04.002

РОЗШИРЕННЯ ВІД ОСНОВНОЇ ДО БЕЗОСНОВНОЇ МОДЕЛІ ЯДЕРНОЇ ОБОЛОНКИ З ХВИЛЬОВОЮ ФУНКЦІЄЮ ХАРТРІ–ФОКА: ЗАСТОСУВАННЯ ДО СТАНІВ З ПОЗИТИВНОЮ ПАРНІСТЮ В ^{19}F

Берун Н. Гафур[1,2], **Азіз Х. Фатах**[3], **Арі К. Ахмед**[1]

[1] *Університет Сулеймані, Коледж освіти, Фізичний факультет, Ірак*

[2] *Науково-дослідний центр, Університет Сулеймані, Ірак*

[3] *Університет Сулеймані, Коледж природничих наук, Фізичний факультет, Ірак*

У цій роботі представлено детальне дослідження низько розташованих станів з позитивною парністю в ядрі ^{19}F шляхом поєднання методів оболонкової моделі з розрахунками Хартрі–Фока (HF). Дослідження систематично поширюється від традиційних просторів на основі ядра (sd, zbm, psd) до повністю неусіченої конфігурації без ядра ($spsdpf$). Реалістичні одночастинкові хвильові функції були згенеровані за допомогою гармонічного осцилятора (HO), параметризацій Вудса-Саксона (WS) та 39 Скірма. Підхід був протестований на широкому наборі спостережуваних величин, включаючи спектри збудження, електромагнітні форм-фактори ($C0$, $C2$, $C4$, $M1$, $M3$, $E2$, $E4$ та $E4 + M5$), ймовірності переходів, магнітні дипольні та електричні квадрупольні моменти, а також енергії зв'язку та середньоквадратичні радіуси зарядів. Розбіжності, про які повідомлялося в попередніх теоретичних роботах, особливо для переходів $M1$ та $C4$ при більших передачах імпульсу, були вирішені за допомогою розширених модельних просторів та уточнених радіальних хвильових функцій. Разом з нашим попереднім дослідженням станів негативної парності в ^{19}F, ці результати дають цілісну картину: систематичні розширення від ядра до відсутності ядра є важливими для точного відтворення як детальних, так і об'ємних ядерних властивостей. Ця єдина структура посилює теоретичне моделювання ^{19}F та закладає основу для майбутніх досліджень ядер у перехідних та деформованих областях за допомогою оболонкових моделей.

Ключові слова: *модель ядерної оболонки; модель без оболонки; хвильова функція Хартрі–Фока; Skyrme Хартрі–Фок; ефективна взаємодія; електромагнітні форм-фактори; енергетичні рівні* ^{19}F